LITHOS 472-473 (2024) 107555

Contents lists available at ScienceDirect

LITHOS

journal homepage: www.elsevier.com/locate/lithos

Geochemical evidence for crustal anatexis during intra-orogenic transcurrent tectonics: Insights from Variscan peraluminous granites from the La Bazana Pluton (Ossa–Morena Zone, Iberian Massif)

Jon Errandonea-Martin [a,*], Fernando Sarrionandia [b], Sonia García de Madinabeitia [a], Aratz Beranoaguirre [c], Manuel Carracedo-Sánchez [a], Idoia Garate-Olave [a], José Ignacio Gil Ibarguchi [a]

[a] Department of Geology, Faculty of Science and Technology, University of the Basque Country (UPV/EHU), 48940 Leioa, Spain
[b] Department of Geology, Faculty of Pharmacy, University of the Basque Country (UPV/EHU), 01006 Vitoria-Gasteiz, Spain
[c] Institute of Applied Geosciences, Karlsruhe Institute of Technology (KIT), 76131 Karlsruhe, Germany

ARTICLE INFO

Keywords:
Granite petrology
Peraluminous
Crustal sources
Mantle-derived magmas
Transcurrent regime

ABSTRACT

Genetic models for granitoid formation in orogenic environments commonly entail varied mantle participation, with differentiation of mafic magmas typifying an end-member model if mantle input dominates over crustal anatexis. By departing from this model, diverse petrogenetic processes and combination thereof could also produce weakly peraluminous compositions in such domains, deriving in opposite implications in crustal evolution (crustal growth vs. reworking). The interpretation may be further complicated if mafic terms or characteristic mineral phases are absent in a certain granitoid suite, as in the case of the Variscan La Bazana Pluton (Ossa–Morena Zone of the Iberian Massif). This pluton, composed by magnesian, alkali-calcic, and weakly- to strongly-peraluminous biotite-bearing monzogranites and magnesian-ferroan, alkali-calcic, and strongly peraluminous two-mica leucogranites, emplaced at 336.3 ± 0.7 Ma (U-Pb in zircon; quadrupole LA-ICP-MS) in an intra-orogenic transcurrent setting where mantle-derived magmatism was predominant. Whole-rock major- and trace-element data (ICP-MS), together with Sr-Nd isotopes (MC-ICP-MS; $^{87}Sr/^{86}Sr_i$ = 0.7077–0.7134; εNd_i = −8.6 ± 0.2) and zircon inheritances (Neoarchean to Ordovician) indicate that the weakly-peraluminous monzogranite parental magmas derived from a heterogeneous crustal source (metagreywackes and felsic metaigneous rocks). The asthenospheric upwelling and intrusion of mantle-derived magmas, together with shear heating, likely caused melting of such crustal lithologies at mid-crustal levels, with the subsequent emplacement and crystallization at 2–3 kbar and 730–780 °C (Ti-in-zircon). The geochemical evolution of these monzogranites can be modelled by 29% fractional crystallization of Pl (~53%) + Bt (~32%) + Qz (~15%) + Ap (0.80%) + Zrn (0.06%) + Mnz (0.04%). By contrast, the coeval strongly peraluminous two-mica leucogranites are not cogenetic with the biotite-bearing monzogranites. Their geochemical composition, with different εNd_i values (from −9.9 to −10.5) for the same SiO_2 contents, suggest that these leucogranites would represent discrete magma pulses derived from partial melting of Ca-poor metapelites. The weakly peraluminous parental magmas of the studied biotite-bearing monzogranites may be considered as S-type, yet not in the sense of exclusively sediment-derived, but as supracrustal, contrary to the nearby I-type (infracrustal) weakly peraluminous counterparts. The obtained results demonstrate that in transcurrent intra-orogenic mantle-dominated settings both addition of new continental crust and reworking of older crustal lithologies may occur concurrently, and that crustal melting may be broader than expected in such environments.

1. Introduction

Granitoids are the prevailing constituent of the upper–middle continental crust and are pivotal for understanding major processes involved in the growth and reworking of the continental crust during orogenesis (Moyen et al., 2017; Rudnick and Gao, 2014). Moreover,

* Corresponding author.
E-mail address: jon.errandonea@ehu.eus (J. Errandonea-Martin).

https://doi.org/10.1016/j.lithos.2024.107555
Received 29 October 2023; Received in revised form 22 February 2024; Accepted 23 February 2024
Available online 28 February 2024

granitic plutons and batholiths are important sources of precious and base metal deposits, where porphyry ores (Cu, Au, Mo, W, Sn and Ag) and lithophile ores (Sn, W, F, Li, Be, Nb, REE, P, U, and Th), are associated with a specific granitoid type (Robb, 2020). Granites (sensu *lato*) can form by diverse processes including differentiation of mafic magmas by assimilation and/or fractional crystallization, partial melting of crustal lithologies, mixing between mantle- and crust-derived magmas, or a combination thereof (Barbarin, 1999; Bonin et al., 2020; Moyen et al., 2021), and therefore, their study is still challenging. The granite composition and the geodynamic setting are related, but the abundance of published geochemical discriminant diagrams highlights the complexity of simplifying their classification (see Bonin et al., 2020 for a review). Moreover, determining source rocks and mechanisms of magmatic evolution in a granitoid intrusion is often not straightforward (e.g. Clemens and Stevens, 2012; Jacob et al., 2021).

In collisional orogens, heat sources required to melt the crust and produce granitic melts may result from 1) thickening of the continental crust and accumulation of radiogenic heat, 2) intrusion of hot basic magmas, 3) rapid exhumation of high metamorphic-grade terrains, 4) thinning of the continental crust and heat conduction from the mantle, and 5) lithospheric-scale shearing (Janoušek et al., 2020). Collisional or post-collisional (muscovite- and cordierite-bearing) granodiorites–leucogranites, of strongly-peraluminous composition, are usually generated by anatexis of metasedimentary rocks of the middle–upper continental crust and they are classified as S-type (supracrustal–sedimentary; Barbarin, 1999; Chappell and White, 1992; Sylvester, 1998; Villaseca et al., 1998). On the contrary, I-type (infracrustal–igneous; Chappell et al., 2012; Clemens et al., 2011) metaluminous to weakly peraluminous (amphibole-bearing and potassic calc-alkaline) granitoids can be formed both in active continental margins (magmatic arcs) and in post-collisional intracontinental extensional environments, being more difficult to classify (Castro, 2020; Gao et al., 2016; Jacob et al., 2021). Furthermore, Castro (2020) proposed a subdivision of these granitoids, distinguishing 'primary' I-type granitoids, derived from differentiation by fractionation of andesitic magmas (directly related to subduction), and 'secondary' I-type granitoids, from water-fluxed melting of older subduction-related igneous rocks placed in the lower crust. More recently, experimental data have demonstrated that this kind of I-type metaluminous to weakly peraluminous granite magmas can be generated also by fractionation of mantle-derived intermediate parental magmas of sanukitoid-vaugneritic affinity (Gómez-Frutos et al., 2023).

Peraluminous granitoids are defined chemically as rocks with molar Al_2O_3 / ($CaO + Na_2O + K_2O$) ratios (A/CNK) greater than unity (Shand, 1943; Zen, 1988), with an excess of Al that leads to the crystallization of characteristic mineral phases such as cordierite, muscovite, almandine-rich garnet, andalusite, sillimanite, topaz, tourmaline and monazite (Bea et al., 1992; Zen, 1988). In terms of petrogenesis, most peraluminous granitoids are generated by partial melting of crustal rocks and may define distinct series controlled by the source rock composition (Barbarin, 1996; Villaseca et al., 1998). Nevertheless, no matter the source of the parental magma, many granitoid types (other than S-type) form magmatic series and tend to evolve towards a weakly peraluminous granite minima (Debon and Le Fort, 1983; Frost et al., 2001). If the composition of the less evolved granitoids in a certain granitoid intrusion is already weakly peraluminous, and more mafic terms are absent, the petrogenetic interpretation and classification, together with the following geodynamic implications can be very diverse (e.g. Bonin et al., 2020; Jacob et al., 2021).

Huge granitoid bodies that emplaced in the Iberian Massif during the Variscan Orogeny are an excellent natural laboratory for granite petrology research. In the southern Iberian Massif, in the so-called Ossa-Morena Zone, the igneous rocks occur in parallel to lithospheric-scale shear zones. Whereas in the Nisa–Alburquerque–Los Pedroches Magmatic Alignment both strongly peraluminous and metaluminous granitoids are abundant (Castro et al., 2023; Errandonea-Martin et al., 2019), to the south of this alignment mantle-triggered magmatism becomes predominant, with metaluminous diorite–granodiorite intrusions (Cambeses et al., 2015, 2019; Casquet et al., 2001; Sarrionandia, 2006). Within the latter, the La Bazana Pluton, exclusively constituted by peraluminous rocks, is an exceptional case study to evaluate the role of mantle- and crust-derived magmas in the generation of peraluminous granites in transcurrent regimes. In this contribution it is presented a detailed petrological study of the La Bazana Pluton, combining new data on whole-rock major- and trace-elements and Sr-Nd isotopes, mineral chemistry, LA-ICP-MS zircon U-Pb geochronology, zircon- and whole-rock-based geothermometry, and a geochemical modelling.

2. Geological setting

The Ossa–Morena Zone (OMZ) corresponds to a continental lithospheric segment of the peri-Gondwanan domain located in the southern Iberian Massif (Fig. 1a,b; e.g. Cambeses et al., 2017, and references therein). This continental terrane was amalgamated to the Central Iberian Zone (CIZ) during the Cadomian Orogeny and subsequently underwent the Cambro–Ordovician extension and the Variscan Orogeny (Bandrés et al., 2004; Eguíluz et al., 2000). This polyorogenic evolution resulted in a complex internal structure, which comprises NW–SE-trending tectonostratigraphic units separated by crustal-scale faults (e.g. Ábalos et al., 2022 and references therein).

The stratigraphic record of the OMZ encloses a late Proterozoic–Lower Paleozoic basement constituted by (meta-) sedimentary and volcanic successions intruded by (meta-) igneous rocks, developed in a continental active margin (López-Guijarro et al., 2008; Rojo-Pérez et al., 2021 and references therein; Sarrionandia et al., 2020). These successions comprise the 3000–4000 m thick Ediacaran record known as 'Serie Negra Group', a pile of meta-sedimentary rocks with interbedded black quartzite layers and volcanic-volcaniclastic deposits (Fuenlabrada et al., 2021; López-Guijarro et al., 2008; Rojo-Pérez et al., 2021; Sánchez-Lorda et al., 2014). The 'Serie Negra Group' is overlain by the Ediacaran–Lower Cambrian Malcocinado Formation, composed of slates, phyllites, arkoses, greywackes, and limestones, with considerable interbedded sub-alkali andesites and basaltic andesites (lava flows), and pyroclastic deposits of varied compositions (Sarrionandia et al., 2020 and references therein). Variably metamorphosed basic–ultrabasic volcanic rocks (amphibolites s.l.), basic–intermediate plutonic rocks (gabbros and diorites) and subordinate acid intrusions accompany the aforementioned successions (Fig. 1a; Bandrés et al., 2004; Henriques et al., 2015; Sánchez-Lorda et al., 2014, 2016). The extensional collapse of the Cadomian Orogen led to a continental rifting setting during the middle-Cambrian–lower-Ordovician, which gave rise to a sequence that overlays unconformably the aforementioned basement (Eguíluz et al., 2000; Sánchez-García et al., 2010; Sarrionandia et al., 2012). This Cambrian–Ordovician sequence contains, from its base to the top, a lower detrital formation, a detrital–carbonate formation, an upper detrital formation, and a rift-related, volcanic–sedimentary complex (Cambeses et al., 2017; Sánchez-García et al., 2010; Sarrionandia et al., 2012). During this rifting a minor acid magmatic event of peraluminous affinity was followed by a major bimodal alkaline one (Fig. 1a; Chichorro et al., 2008; Díez Fernández et al., 2014; Sánchez-García et al., 2010; Sarrionandia et al., 2012; Solá et al., 2008). Silurian to Lower Devonian deposits that overly paraconformably the Ordovician sequences consist mainly of argillaceous black shales with interbedded siliceous slates and black cherts, which precede the early Carboniferous synorogenic flyschoidal and molassic succession. Widespread volcanism accompanied the synorogenic successions deposited in shallow marine intracontinental basins (Sarrionandia et al., 2023).

2.1. Variscan magmatism in the Ossa–Morena Zone

Carboniferous Variscan magmatism occurred at ca. 350–320 Ma in the OMZ (e.g. Cambeses et al., 2019; Rodríguez et al., 2022). It arises

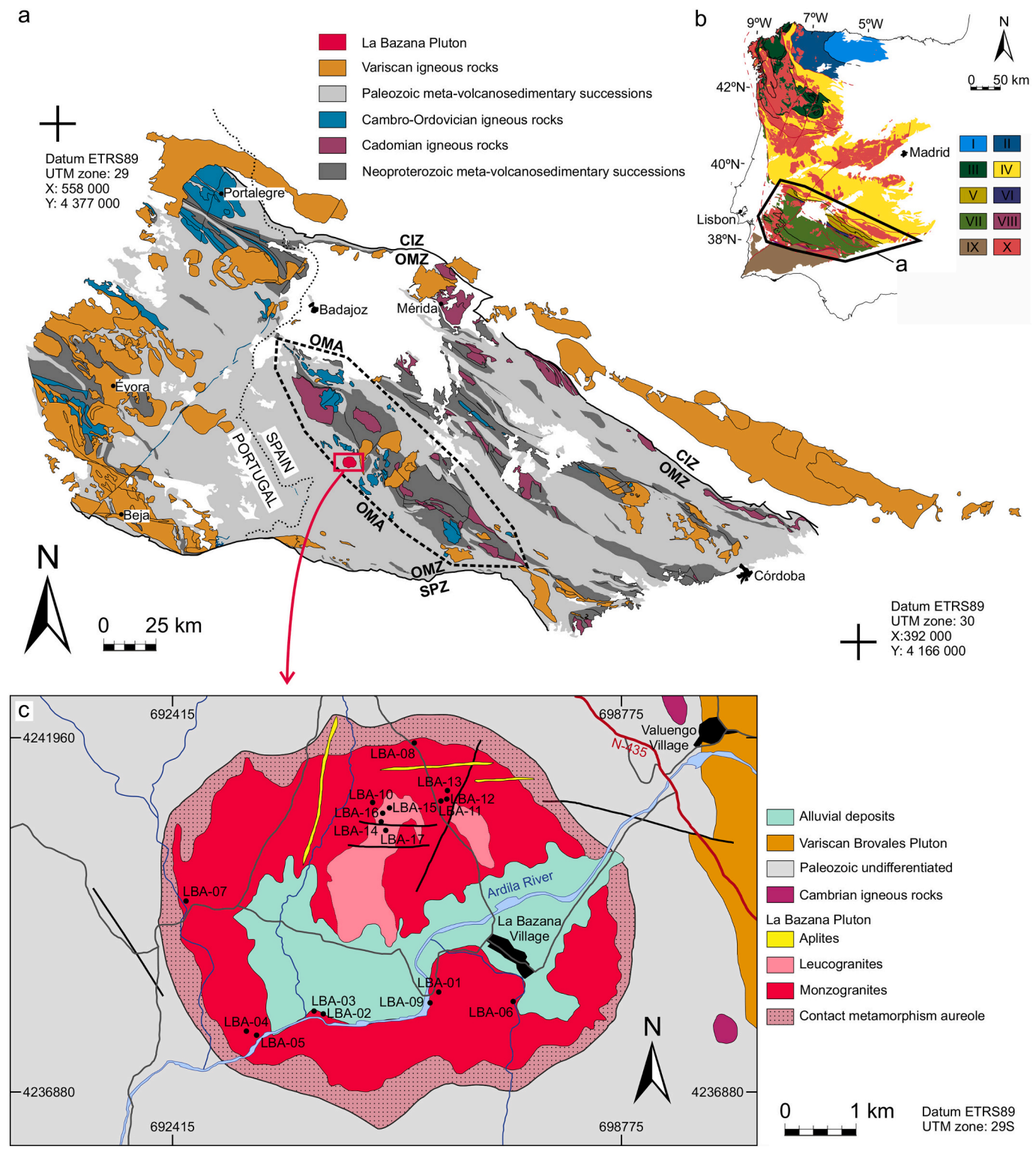

Fig. 1. (a) Regional geological map of the Ossa-Morena Zone (OMZ); CIZ: Central Iberian Zone; OMA: Olivenza–Monesterio Antiform. (b) Geological map of the Iberian Massif: I: Cantabrian Zone, II: West Asturian–Leonese Zone, III: Galicia–Trás-os-Montes Zone, IV: CIZ, V: Obejo–Valsequillo–Puebla de la Reina Domain; VI: Coimbra–Córdoba Shear Zone; VII: OMZ, VIII: Beja–Acebuches Ophiolite; IX: South Portuguese Zone, X: Variscan granitoids. (c) Detailed geological map of the La Bazana Pluton after Fernández Carrasco et al. (1981).

throughout NW–SE trending magmatic alignments and comprises extensive plutonism accompanied by both explosive and effusive volcanic activity (e.g. Cambeses et al., 2015, 2019; Rodríguez et al., 2022; Sarrionandia et al., 2023). This widespread plutonism includes 'calc-alkaline' metaluminous diorites–granodiorites, associated with minor gabbros and tonalites, and peraluminous granite–leucogranites (Fig. 1a; e.g. Cambeses et al., 2015, 2019; Ordoñez-Casado et al., 2008; Pereira et al., 2015; Rodríguez et al., 2022; Sarrionandia, 2006). The oblique convergence of continental terrains along the northern Gondwana margin during the Carboniferous resulted in the Variscan transcurrent

tectonics that favored local transpressional/transtensional regimes (Ábalos et al., 1991; Eguíluz et al., 2000). These transcurrent tectonics played an important role in magma generation and transport during this period, with some intrusions associated with transpression (e.g. Romeo et al., 2006; Tornos et al., 2006) and others to transtension (e.g. Cambeses et al., 2015, 2019). The Olivenza–Monesterio Antiform (OMA) encompasses several Variscan metaluminous (to slightly peraluminous) 'calc-alkaline' plutons in the central part of the OMZ (Fig. 1a). Most of these plutons constitute epizonal inversely zoned bodies composed of mafic–ultramafic cores (gabbros–dioritoids) and more felsic rims (tonalites–granodiorites–granites) (Cambeses et al., 2015, 2019; Casquet et al., 2001; Ordoñez-Casado et al., 2008; Sarrionandia, 2006). They have mantle affinities with metaluminous (to slightly peraluminous) compositions, and have been interpreted as a result of 1) contamination of mantle-derived magmas by crust-derived components, and subsequent fractional crystallization (e.g. Cambeses et al., 2015, 2019; Casquet et al., 2001), or 2) melting of an enriched mantle source and subsequent differentiation by fractional crystallization of the basaltic parental magmas (e.g. Sarrionandia, 2006). The La Bazana Pluton, in the southern limb of the OMA, represents a singular exception to this plutonism (Fig. 1a; e.g. Fernández Carrasco et al., 1981; Flecha et al., 2006; Galadí-Enríquez et al., 2003).

3. Materials and methods

Among the collected 25 rock samples, 17 were selected for the present study: 13 biotite-bearing monzogranites and 4 two-mica leucogranites (sample location in Fig. 1 and Supplementary Table 1). Electron Microprobe (EMP) analyses (results in Supplementary Tables 2, 3 and 4) were performed at the Spanish National Centre for Electron Microscopy (ICTS) (Complutense University of Madrid), whereas the rest of analytical procedures were carried out in the Geochronology and Isotope Geochemistry – SGIker Facility of the University of the Basque Country (UPV/EHU). These procedures include elemental analyses in zircon and monazite by Laser Ablation Inductively Coupled Plasma Mass Spectrometry (LA-ICP-MS) (results in Supplementary Tables 5 and 6), U–Th–Pb isotopic study on zircon by Quadrupole-based LA-ICP-MS (complete data in Supplementary Table 7), whole-rock elemental concentration determinations by ICP-MS (Table 1), and whole-rock Sr-Nd isotopic analyses (Table 2) by Multicollector ICP-MS (elemental Sm and Nd concentrations by Isotope Dilution and Multicollector ICP-MS). Analytical conditions for each method are specified in the 'Materials and Methods' file of the electronic supplementary material.

4. Field relationships and petrography

The La Bazana Pluton is a roughly circular granitic massif of ~20 km^2 that intrudes into Cambrian metasediments and metavolcanic rocks, crosscutting the main Variscan tectonic structures (Fig. 1c). This intrusion generated a metamorphic aureole of up to 250 m thick defined by andalusite-bearing mica-schists (e.g. Fernández Carrasco et al., 1981; Galadí-Enríquez et al., 2003). The contact with the host metasedimentary rocks varies from sharp, showing gentle to moderate dipping, to locally gradational, with injections into the host rocks. According to Galadí-Enríquez et al. (2003), the foliation observed in the host metasediments, and the locally observed magmatic foliation parallel to the contact with the host rocks, would reflect a dome-shape structure of this intrusion.

The most remarkable rock-type in the La Bazana Pluton is a biotite-bearing monzogranite that encompasses ~90% of the exposed massif. Minor leucogranites that show liquid-liquid relationships with the monzogranites and scattered aplite-dykes that are intrusive to the mentioned rocks complete the magmatic assemblage (Figs. 1c and 2a-d). Magmatic microgranular enclaves and pelitic enclaves are rare in the monzogranites and are absent in the leucogranites. The monzogranites show medium- to coarse-grained hypidiomorphic seriated texture, since K-feldspar phenocrysts (< 3 cm) are rare (Fig. 2e). Its modal compositions are quite homogeneous throughout the pluton, with quartz (26–34%), K-feldspar (25–30%), plagioclase (25–30%), biotite (10–15%) and muscovite (< 5%) as main rock-forming minerals, plus accessory apatite, zircon and monazite. Close to the leucogranites, the monzogranite may display local varieties that show slightly lower biotite (7–11%) and higher muscovite (4–8%) proportions. K-feldspar shows a perthitic character, ranging from subhedral to interstitial, and contains abundant inclusions of several mineral phases (mainly plagioclase, biotite, apatite), whereas plagioclase is mainly euhedral and shows several growth stages and concentric oscillatory zoning. Biotite and muscovite occur either as euhedral single flakes (up to 3 mm) or constituting biotite-muscovite aggregates, showing inclusions of zircon, monazite and apatite in the case of some biotite crystals (Fig. 2e).

In contrast with the biotite-bearing monzogranites, the leucogranites of the La Bazana Pluton exhibit an equigranular fine-grained texture, and are heterogeneous in terms of modal composition, with higher quartz (33–42%), K-feldspar (30–40%) and muscovite (7–13%), and lower plagioclase (20–25%) and biotite (< 4%) proportions concerning the monzogranites (Fig. 2f). Accessory mineralogy includes apatite, monazite, tourmaline and magnetite. In the case of the most prominent outcrops, these leucogranites show notably higher muscovite (up to 15%) and lower biotite (< 1%) proportions (± chlorite, epidote), and a characteristic pinkish-yellowish color that evidences hydrothermal alteration.

5. Mineral chemistry

5.1. Feldspars and micas

The composition of non-perthitic K-feldspar varies in the range Or_{86}–Or_{93}, with slightly higher K_2O contents in the case of leucogranites compared with those of monzogranites. Overall, P_2O_5 contents of K-feldspar are similar in both rock types, with values in the range of 0.06 and 0.41 wt% (Supplementary Table 2). Plagioclase from monzogranites is andesine–oligoclase (Ab_{59}–Ab_{90}), whereas that from leucogranites is mainly albite (± oligoclase; Ab_{84}–Ab_{94}). Well-developed plagioclase crystals from monzogranites display chemical zoning with an increase of Ab proportion from core to rim. Contrary to K-feldspar, plagioclase from leucogranites show higher P_2O_5 contents than those from monzogranites (up to 0.45 wt%; Supplementary Table 2; Supplementary Fig. 1). In the latter, P_2O_5 contents increase as differentiation proceeds, roughly in K-feldspar (up to 0.36 wt%) and more evidently in plagioclase (up to 0.33 wt%).

Biotite compositions plot at the boundary between peraluminous and calc-alkaline fields of magmatic series discrimination diagrams (Supplementary Fig. 1). They show similar Al_{total} values in both rock units (1.48–1.64 apfu), but higher mg# ($Mg/[Mg + Fe^{2+}]$) and TiO_2 contents in the monzogranites (up to 0.50 apfu and 3.27 wt%, respectively). Biotite from leucogranites displays higher F contents (up to 0.40 wt%), which increase also with differentiation in biotite from the monzogranites (contrary to mg#, Supplementary Table 3). Muscovite compositions project into the primary field of the Mg–Ti–Na classification diagram (Supplementary Fig. 1), showing slightly lower Al_{total} values (average of 2.57 apfu) and higher TiO_2 contents (1.53 wt%) in the monzogranites (Supplementary Table 3).

5.2. Accessory minerals

Analyzed monazite crystals display little or no chemical variation within the biotite-bearing monzogranites from the La Bazana Pluton (Supplementary Tables 4 and 5), showing monazite *s.s.* compositions based on the monazite ($2REEPO_4$) – cheralite ($CaTh(PO4)_2$) – huttonite ($2ThSiO_4$) classification diagram (Supplementary Fig. 1). Accordingly, SiO_2, CaO, Th, and U contents are relatively low (~0.118 wt%, ~1.41 wt %, < 74,200 ppm, and ~ 1.29 ppm, respectively), and those of La, Ce,

Table 1
Major- (wt%) and trace-element (ppm) whole-rock geochemical analyses of monzogranites and leucogranites from La Bazana.

Sample	LBA-01	LBA-02	LBA-03	LBA-04	LBA-05	LBA-06	LBA-07	LBA-08	LBA-09	LBA-10	LBA-11	LBA-12	LBA-13	LBA-14	LBA-15	LBA-16	LBA-17
Unit	Mzgr	Mzgr	Mzgr	Mzgr	Mzgr	Mzgr	Mzgr	Mzgr	Mzgr	Mzgr	Mzgr	Mzgr	Mzgr	Lcgr	Lcgr	Lcgr	Lcgr
SiO_2	69.9	67.87	68.87	67.73	68.55	68.81	68.31	67.37	68.48	70.08	71.16	69.94	71.84	72.9	73.72	73.02	72.96
TiO_2	0.3	0.31	0.27	0.36	0.36	0.33	0.35	0.39	0.34	0.28	0.25	0.26	0.26	0.12	0.09	0.09	0.13
Al_2O_3	14.97	15.23	14.8	15.15	15.84	15.71	15.48	15.79	16.01	15.9	15.73	15.7	15.35	15.13	15.18	15.05	15.31
CaO	1.83	1.93	1.72	1.9	2.16	1.77	2.2	2.36	2.68	1.06	1.34	1.67	1.37	0.1	0.16	0.35	0.72
FeO^t	2.29	2.31	2.04	2.16	2.35	2.19	2.44	2.6	2.12	1.94	1.61	1.81	1.82	1.28	1.03	2.15	1.23
K_2O	4.7	4.75	4.85	4.45	4.94	4.63	4.81	4.56	4.55	4.77	4.85	4.86	4.92	5.33	5.48	4.47	4.28
MgO	0.82	0.86	0.77	1.03	0.91	0.94	0.95	1.12	0.9	0.71	0.64	0.69	0.74	0.25	0.07	0.21	0.34
MnO	0.08	0.07	0.04	0.04	0.07	0.08	0.03	0.04	0.08	0.09	0.06	0.08	0.07	0.02	<MDL	<MDL	0.02
Na_2O	3.3	3.39	3.28	3.71	3.08	3.33	3.11	3.2	3.39	3.32	3.6	3.53	3.49	3.51	2.61	2.66	3.44
P_2O_5	0.19	0.2	0.2	0.21	0.14	0.13	0.13	0.14	0.14	0.16	0.17	0.16	0.21	0.2	0.22	0.28	0.32
LOI	1.02	1.12	1.21	1.27	1.12	1.13	1.46	1.2	1.54	1.22	1.05	0.95	0.96	1.09	1.53	1.47	1.11
Total	99.4	98.04	98.05	98.01	99.52	99.05	99.27	98.77	100.23	99.53	100.46	99.65	100.52	99.93	100.09	99.75	99.86
Ba	542	588	601	557	710	476	605	560	504	361	453	431	376	177	238	193	233
Co	113	98.2	107	91.7	87.1	95.4	87.6	97.8	60.5	98	106	69.6	101	105	100	68.2	64.7
Cr	17	17.1	14.4	20	17.8	16.6	17.5	18.2	15.4	12.4	10.6	11	11.4	3.18	1.01	1.48	3.79
Cs	9.1	8.07	7.84	6.42	8.16	13	3.73	5.44	13.9	19.7	12.2	9.38	18.4	4.37	5.9	5.4	8.54
Ga	20.6	19.9	17.5	18.4	19.4	18.9	18.1	19.9	18.8	20.1	17.4	17.4	19.9	16.7	18.9	19.8	14.6
Hf	4.21	4.11	3.77	4.47	4.2	4.08	4.32	4.3	3.76	3.3	3.12	3.26	3.12	1.74	1.51	1.54	1.86
Ni	37.4	39.3	31.3	26	18.3	19.3	4.21	7.99	1.1	3.34	<MDL	3.02	15.6	21.8	10.2	<MDL	<MDL
Nb	14.6	13.3	12.5	13.2	14.3	13.3	13.1	14.2	13.8	16.2	14.5	14.2	15.5	14.8	19.9	17.8	14.6
Pb	33.9	35.1	32.4	30.2	36	34.2	28.4	32.2	35.3	31.8	36.4	38.5	35.5	34.2	21.1	18.5	40
Rb	231	232	232	194	231	231	215	209	246	269	261	250	250	249	320	280	255
Sc	8.19	8	6.55	8.19	7.96	7.69	7.58	8.12	7.83	8.8	6.45	6.31	8.75	6.26	5.1	5.36	5
Sn	3.4	3.48	3.43	2.95	3.32	3.98	4.04	4.6	4.03	5.47	4.99	3.67	6.01	3.53	6.2	6.52	3.78
Sr	139	148	142	171	160	129	149	146	141	104	123	115	108	86.1	71.5	68.3	92.3
Ta	2.67	2.14	2.15	1.8	2.7	3.26	2.61	2.69	2.9	4.67	4.35	3.71	3.72	3.64	6.68	5.23	4.36
Th	12.5	12.1	11.1	13.4	14.1	12.5	13.1	14.2	12.5	9.51	9.1	9.56	8.55	3.42	1.79	2.03	3.56
U	2.46	2.12	2.51	9.13	3.06	2.24	3.2	2.72	3.05	3.41	2.87	2.55	2.96	5.34	3.23	4.87	3.69
V	57	54.9	48.1	64	59.3	51.5	57.1	61.6	51.9	45.6	36.8	38	41.1	11.5	9.65	10.3	12.8
Y	24.9	23	22.8	24	27.5	23	27.2	26.9	27.5	21.7	23	22.5	21.7	18	15.5	15.3	17
Zn	47.1	40.3	14.4	9.06	45.3	39.2	2.89	7.13	37	36.3	126	35.5	46.9	<MDL	<MDL	<MDL	<MDL
Zr	128	131	118	139	143	132	137	142	123	104	98.4	102	97.8	47	36.9	37.8	50.8
La	26.6	25.9	23.7	28.5	29.2	26.3	28.2	29.4	26.1	20.1	19	20.3	18.4	8.77	6.07	6.25	9.04
Ce	54.9	53.4	49	59.4	60.9	54	58.4	60.8	53.9	41.7	39.4	41.9	38.2	18	12.8	12.7	18.4
Pr	6.51	6.29	5.72	7.03	7.35	6.55	7.03	7.43	6.54	5.09	4.83	5.13	4.58	2.21	1.52	1.48	2.23
Nd	24.1	23.2	21.8	26.1	26.7	24	25.8	26.9	23.7	18.8	17.2	18.6	16.8	8.01	5.55	5.43	7.9
Sm	5.03	4.93	4.41	5.6	5.57	4.91	5.47	5.47	5.09	4.24	3.75	3.89	3.92	2.13	1.36	1.39	1.94
Eu	0.896	0.916	0.852	0.982	1.06	0.908	0.993	1.04	0.916	0.734	0.72	0.778	0.751	0.429	0.403	0.327	0.44
Gd	4.55	4.14	3.74	4.68	4.9	4.04	4.62	4.74	4.37	3.46	3.4	3.32	3.2	2.03	1.46	1.49	2
Tb	0.691	0.643	0.627	0.706	0.728	0.63	0.726	0.723	0.662	0.546	0.537	0.577	0.536	0.373	0.328	0.316	0.387
Dy	3.72	3.5	3.43	3.72	3.87	3.46	3.86	3.98	3.82	3.13	3.28	3.19	3.15	2.44	2.19	2.04	2.39
Ho	0.569	0.536	0.521	0.554	0.604	0.512	0.594	0.579	0.591	0.467	0.505	0.492	0.479	0.384	0.321	0.3	0.348
Er	1.91	1.74	1.73	1.9	1.92	1.62	1.98	1.93	1.9	1.53	1.61	1.62	1.59	1.14	1.05	0.937	1.09
Tm	0.33	0.299	0.313	0.321	0.353	0.281	0.355	0.33	0.342	0.281	0.285	0.279	0.277	0.195	0.173	0.177	0.2
Yb	1.94	1.83	1.8	1.81	1.97	1.69	2	1.94	2.02	1.73	1.66	1.62	1.61	1.18	1.01	0.978	1.11
Lu	0.35	0.326	0.318	0.322	0.357	0.315	0.345	0.331	0.348	0.28	0.288	0.3	0.274	0.188	0.163	0.169	0.185

Mzgr: monzogranite; Lcgr: leucogranite.
Method Detection Limit (MDL) defined in García de Madinabeitia et al. (2008).

Table 2
Whole-rock Sr-Nd isotopic compositions of monzogranites and leucogranites from La Bazana.

Sample	LBA-01	LBA-02	LBA-05	LBA-06	LBA-07	LBA-08	LBA-11	LBA-12	LBA-13	LBA-14	LBA-16	LBA-17
Unit	Mzgr	Mzgr	Mzgr	Mzgr	Mzgr	Mzgr	Mzgr	Mzgr	Mzgr	Lcgr	Lcgr	Lcgr
Rb (ppm)	231	232	231	231	215	209	261	250	250	249	280	255
Sr (ppm)	139	148	160	129	149	146	123	115	108	86.1	68.3	92.3
$^{87}Rb/^{86}Sr$	4.822	4.547	4.188	5.196	4.185	4.152	6.160	6.314	6.721	8.407	11.93	8.030
$^{87}Sr/^{86}Sr$	0.732648	0.729679	0.729505	0.733080	0.729407	0.728424	0.738257	0.743148	0.739351	0.752470	0.765541	0.750524
2σ error (abs)	0.000007	0.000008	0.000007	0.000008	0.000007	0.000006	0.000007	0.000007	0.000008	0.000007	0.000008	0.000007
$^{87}Sr/^{86}Sr_i$	0.7100	0.7083	0.7098	0.7086	0.7097	0.7089	0.7093	0.7134	0.7077	0.7129	0.7094	0.7127
Sm (ppm)	4.19	4.26	4.49	4.53	4.69	4.81	3.29	3.26	3.56	1.62	1.25	1.83
Nd (ppm)	21.1	21.4	22.4	22.9	23.4	24.2	15.9	15.6	17.4	6.50	4.96	7.63
$^{147}Sm/^{144}Nd$	0.1202	0.1205	0.1210	0.1198	0.1215	0.1203	0.1254	0.1264	0.1239	0.1506	0.1519	0.1450
$^{143}Nd/^{144}Nd$	0.512033	0.512030	0.512032	0.512030	0.512031	0.512036	0.512030	0.512033	0.512035	0.512022	0.512004	0.512020
2σ error (abs)	0.000007	0.000008	0.000008	0.000008	0.000008	0.000006	0.000008	0.000007	0.000006	0.000009	0.000008	0.000009
$^{143}Nd/^{144}Nd_i$	0.511769	0.511765	0.511766	0.511766	0.511764	0.511771	0.511754	0.511755	0.511762	0.511691	0.51167	0.511701
εNd_i	−8.53	−8.6	−8.58	−8.57	−8.62	−8.47	−8.81	−8.79	−8.65	−10.05	−10.45	−9.85

Mzgr: monzogranite; Lcgr: leucogranite.
Isotopic ratios age-corrected to the newly obtained U-Pb zircon age of 336 Ma.

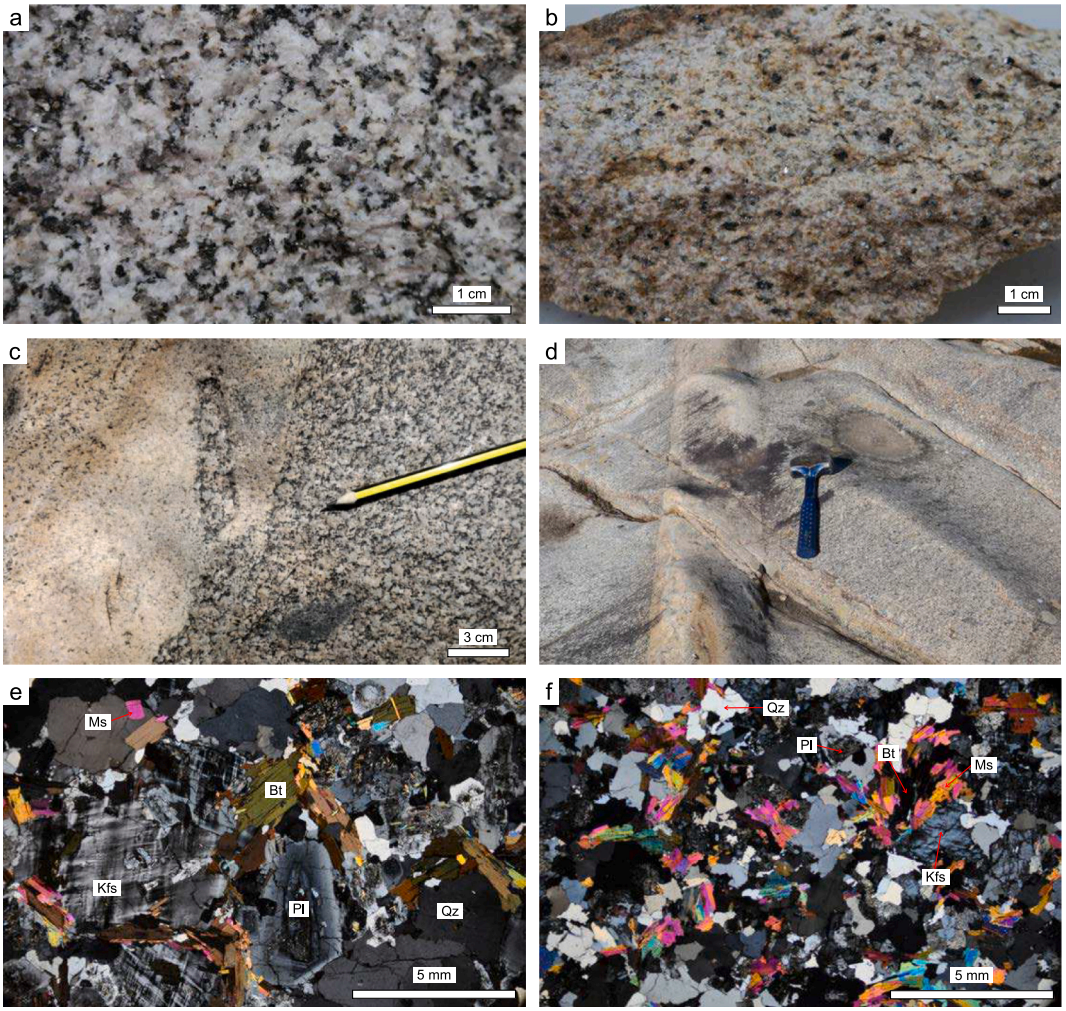

Fig. 2. (a) Section of a representative sample of biotite-bearing monzogranite from La Bazana, where biotite is the only discernable mafic mineral phase. (b) A representative two-mica leucogranite sample from La Bazana showing both biotite and muscovite flakes. (c) Detailed picture showing liquid-liquid relationships between studied monzogranites and leucogranites. (d) Aplitic dyke crosscutting a monzogranite boulder. (e) Monzogranite and (f) leucogranite optical photomicrographs in cross-polarized light showing coarse grain size in monzogranites, higher plagioclase proportion in monzogranites, and higher muscovite abundance in leucogranites. Bt: biotite; Kfs: K-feldspar; Ms: muscovite; Pl: plagioclase; Qz: quartz.

Nd, and Y are high (up to 18.84, 34.89, 15.10, and 2.82 wt%, respectively), with ΣREE contents in the range of 590,000–772,000 ppm. Chondrite-normalized REE patterns (normalization values from McDonough and Sun, 1995) show characteristic decreasing trends, with marked negative Eu anomalies (average Eu/Eu* of 0.26) and higher fractionation degrees in the case of heavy REE (HREE; average Gd_N/Lu_N = 72.8) compared with light REE (LREE; average La_N/Sm_N = 4.41) (Supplementary Fig. 1).

Zircon elemental compositions do not disclose differences or groups among analyzed crystals from the studied monzogranites (Supplementary Table 6). They show variable Th/U ratios (0.020–0.878), Hf contents (from ~ 7500 to 20,000 ppm), and ΣREE values (368–5558 ppm), while Ti contents are fairly homogeneous (1.87–6.66 ppm). In chondrite-normalized plots (normalization values from McDonough and Sun, 1995), HREE of zircon display homogeneous increasing trends (leading to typical small La_N/Lu_N ratios; < 0.008), contrary to LREE, which show positive Ce and negative Eu anomalies that are stronger in the less enriched crystals (Supplementary Fig. 1).

Apatite group minerals show similar compositions in all cases, with high F (1.03–1.73; apfu) and low Cl (< 0.072; apfu) contents that lead to their classification as fluorapatite (Supplementary Tables 4). MnO contents in apatite vary in the range of 0.544–1.73 wt%, which are slightly higher than those of FeO (0.006–0.573).

6. Zircon geochronology

Zircon grains were separated from a poorly evolved biotite-bearing monzogranite sample (LBA-02) and were analyzed by LA-ICP-MS after a careful study of morphological characteristics. Zircon crystals are euhedral, 80–240 μm long, and commonly show magmatic zoning (Fig. 3a). Inherited cores are evident in some grains, and others contain inclusions of smaller mineral phases (< 10 μm; Fig. 3a). A total of 189 analyses were performed and 18 of them were discarded due to high analytical uncertainties. The remaining 171 results show concordance between 54 and 103%, out of which 129 spots have discordances < 10% and 78 of them < 5% (Fig. 3b; Supplementary Table 7). The 129 results with concordance > 90% are considered adequate for the age calculations. These define 5 peaks in the radial plot obtained for $^{206}Pb/^{238}U$ ages and corresponding analytical uncertainties (Fig. 3c): Peak #1, with an age of 330.7 ± 0.4 Ma defined by 47 analyses, shows limited dispersion; Peak #2, defined by 35 analyses slightly more dispersed yields a value of 497 ± 1 Ma; Peak #3 includes 27 analyses that provide an age of 633 ± 1 Ma; and Peaks #4 and #5 only include 13% of the results and represent more dispersed older ages. The dispersion of age data older than 400 Ma is practically continuous, which hinders the determination of representative ages and suggests the presence of inherited cores or zircon domains that could be affected by Pb-loss. After discarding the most discordant data and excluding those out of the 2σ

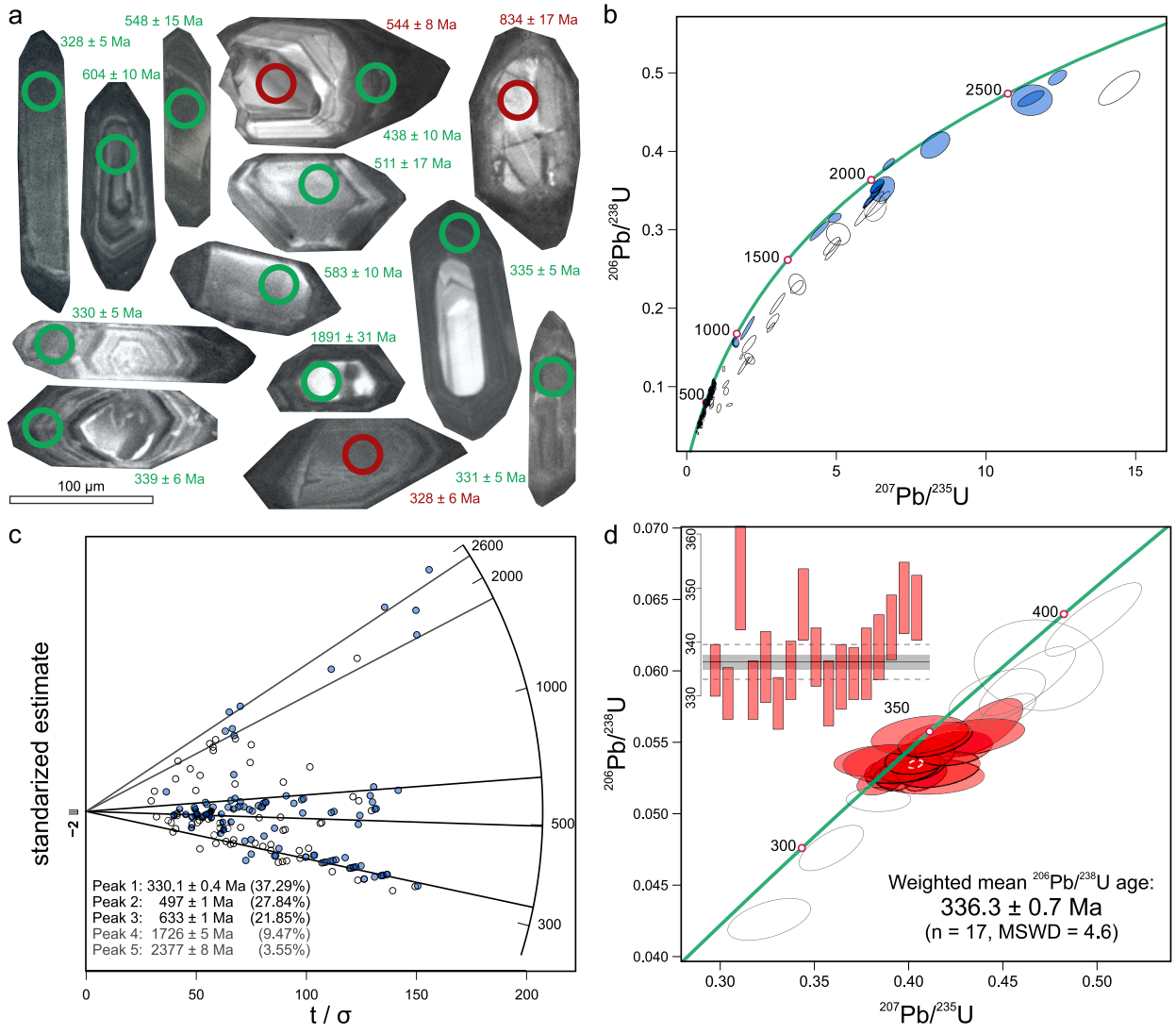

Fig. 3. (a) Cathodoluminescence images of representative zircon crystals separated from a monzogranite sample of La Bazana (green ellipses represent analyses with discordances of < 10%, and red ellipses of > 10%). (b) U-Pb concordia diagram for analyzed zircon grains, with filled ellipses representing analyses of > 95% of concordance within the complete dataset. (c) Radial plot of $^{206}Pb/^{238}U$ ages and respective errors that lead to 5 statistically calculated age peaks. (d) Zoom of the U-Pb concordia diagram in the youngest age peak, with weighted-mean $^{206}Pb/^{238}U$ diagram and age results (weighted mean age calculated based on analyses with concordance > 95%). (For interpretation of the references to color in this figure legend, the reader is referred to the web version of this article.)

error (of the mean) cut-off, the remaining forty-five analyses with ages younger than 400 Ma define a weighted mean $^{206}Pb/^{238}U$ age of 336.3 ± 0.7 Ma (n = 17, MSWD = 4.6) illustrated in Fig. 3d. This Visean (lower–middle Carboniferous) age is interpreted as that of the crystallization of the studied biotite-bearing monzogranites, whereas the older preserved ages, ranging from ~450 Ma to ~700 Ma (and several > 1000 Ma), would indicate Cambro–Ordovician (peak at ca. 497 Ma), Neoproterozoic (peak at ca. 633 Ma), and Meso- Paleo-Proterozoic inheritances (Supplementary Table 7).

7. Whole-rock geochemistry

7.1. Major- and trace-elements

Monzogranites from La Bazana display high silica contents (67–72 wt%) and maficity parameter values of 41–69 ([B] parameter of Debon and Le Fort, 1983; Fig. 4a,b) (Table 1). Studied monzogranites are principally alkali-calcic, with MALI values of Frost et al. (2001) between 5.3 and 7.1. The [P] and [Q] multicationic parameters (Debon and Le Fort, 1983) vary from −61 and 139 to −25 and 176, respectively (Fig. 4a,c). The set of samples comprises low- to moderately peraluminous compositions defined by A/CNK values (Shand, 1943) in the range 1.04–1.27 (in molar proportions; Fig. 4d). They show magnesian compositions (Frost et al., 2001), and depict a slight subhorizontal trend with FeOt / (FeOt + MgO) values nearly at 0.72. Values of K/(Na + K) (in millications) vary from 0.44 to 0.51, and overall, P_2O_5 (< 0.2 wt%) and K_2O (< 5 wt%) display positive correlation with SiO_2. The studied monzogranites display a high Rb/Ba and Rb/Sr ratios of up to 0.75 and 2.6, respectively, with a clear decreasing trend of the K/Rb ratio as differentiation proceeds. Large Ion Lithophile Elements (LILE) show

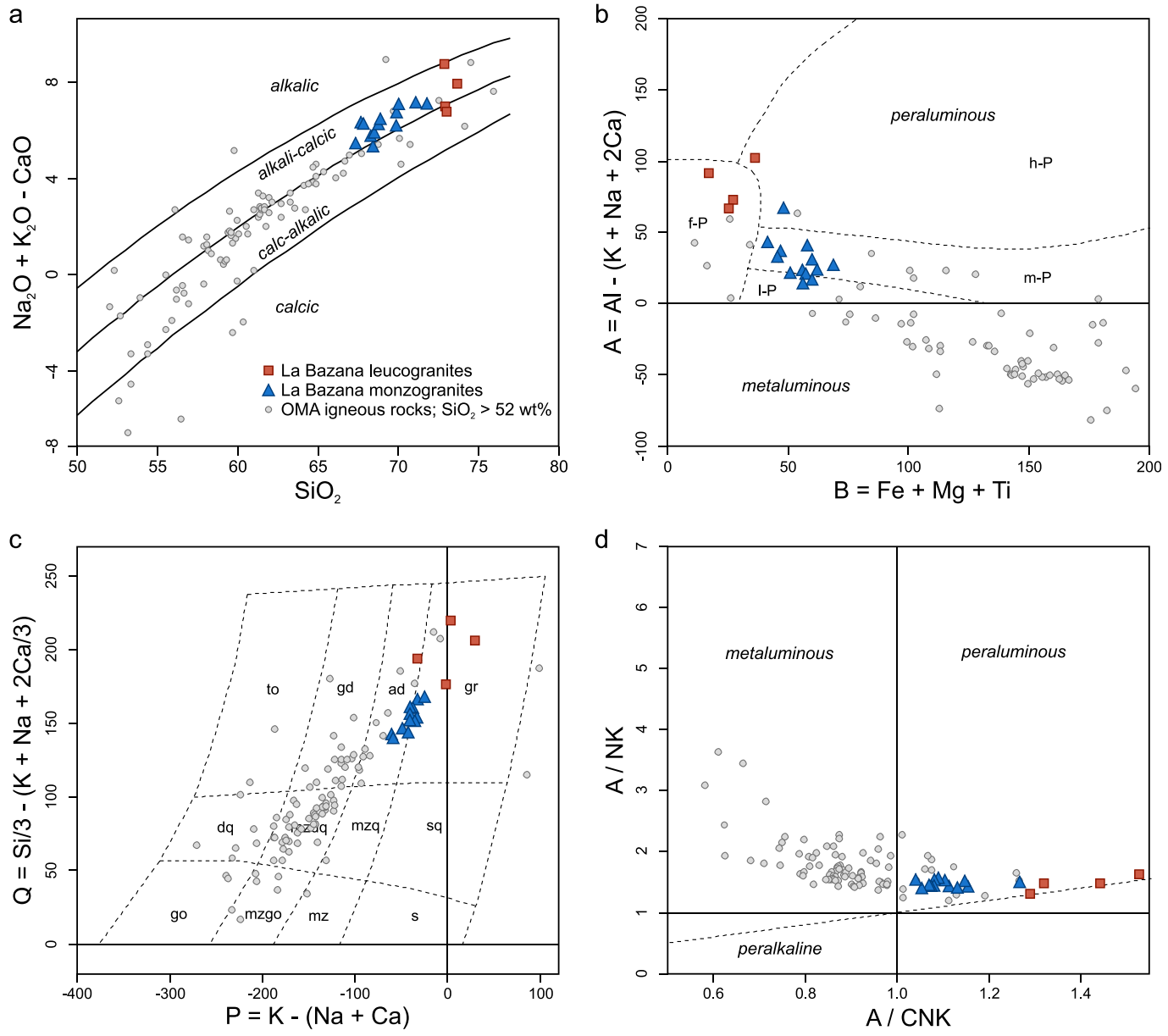

Fig. 4. Whole-rock classification diagrams for La Bazana biotite-bearing monzogranites and two-mica leucogranites: (a) SiO_2 vs. MALI diagram (Frost et al., 2001) (both parameters in oxide weight %). (b) B–A diagram of Debon and Le Fort (1983) modified by Villaseca et al. (1998) (both parameters in millications). (c) P–Q diagram of Debon and Le Fort (1983) (both parameters in millications). (d) A/CNK vs. A/NK diagram (Shand, 1943) (both parameters in molar proportions). Analyses of intermediate–acid Variscan igneous rocks from the OMA are shown also for comparison (data taken from Cambeses et al., 2015, 2019; Casquet et al., 2001; Sarrionandia, 2006).

higher contents than the Upper Continental Crust (UCC) of Rudnick and Gao (2014), except for Ba, with slightly lower contents, and Sr, that shows a marked negative anomaly (Fig. 5a). Whereas Ba and Sr behave as compatible elements, Rb and Cs contents increase from the less acidic monzogranites to the most evolved samples (Table 1). Some High Field Strength Elements (HFSE), namely Nb, Y, U, Th, Pb, Sn, and Ga, display analogous contents to those of the UCC, while others (Zr, Hf, La, Ce, Sc) show lower contents, and Ta displays a striking positive anomaly (Fig. 5a). Most analyzed trace elements display fairly good trends from the less siliceous to the most differentiated terms, with decreasing tendencies for Sc, Zr, Hf, Th, and Y, and increasing ones for Sn, Nb, Ta, U, and Pb (Supplementary Fig. 2). Total REE contents decrease in monzogranites from 146 to 94 ppm with increasing SiO_2. Chondrite-normalized REE patterns are segmented (almost flat for Ho, Er, Tm Yb and Lu), and display an average fractionation degree of 9.27 (La_N/Yb_N) (Fig. 5b). All samples display negative Eu anomalies, with an average Eu/Eu* of 0.61.

Two-mica leucogranites from La Bazana display compositional differences when compared with the monzogranites. SiO_2 contents are higher (73.7 wt%) and [B] parameter values lower (17–36, in millications) (Fig. 4a,b). MALI values (6.8–8.7) cover the range of the alkali-calcic area, and both [P] and [Q] parameters reach up to values of 29 and 220, respectively (Fig. 4a,c). The samples are strongly peraluminous, with A/CNK values up to 1.53, and all fall into the 'highly-' and 'felsic-peraluminous' fields of the B-A diagram defined by Villaseca et al. (1998) (Fig. 4b,d). Leucogranite samples display variable FeOt / (FeOt + MgO) ratios trespassing vertically from the magnesian into the ferroan field of Frost et al. (2001). The K/(Na + K) ratios in leucogranites (up to 0.58) are higher than in the studied monzogranites, similar to P_2O_5 contents that vary from 0.20 to 0.32 wt% (Table 1). The UCC-normalized multielement patterns show that leucogranites are richer in Rb, P, U, Nb and Ta than the monzogranites, while the opposite occurs for Ba, Sr, Th, Hf, Zr and Y (Fig. 5a). REE data also substantiate the compositional differences between the studied monzogranites and leucogranites: total REE contents of 34–48 ppm, average fractionation degree of 4.75 in chondrite-normalized REE diagrams, and lower average Eu/Eu* of 0.72 in the leucogranites (Fig. 5b).

7.2. Whole-rock Sr-Nd isotopes

Nine representative biotite-bearing monzogranites and three two-mica leucogranites were selected for the whole-rock Sr-Nd isotopic study. Measured isotopic ratios were age-corrected to the U-Pb zircon crystallization age of 336 Ma obtained for the studied monzogranites (Table 2). $^{87}Rb/^{86}Sr$ ratios increase from the less siliceous monzogranite up to the most differentiated leucogranite, with most of the monzogranites showing fairly homogeneous $^{87}Sr/^{86}Sr_i$ ratios of 0.7077–0.7100 (Fig. 6a; Table 2). The leucogranite sample LBA-16, located closest to the contact with the monzogranites, shows the lowest $^{87}Sr/^{86}Sr_i$ value among these rocks (0.7094), in the range of those measured in the monzogranites. The remaining leucogranitic samples show higher $^{87}Sr/^{86}Sr_i$ values (0.7127–0.7129), similar to that of the most radiogenic monzogranite, in fact, located close to the contact with the small leucogranitic body (Figs. 1 and 6a; Table 2). Sm-Nd systematics reinforce compositional differences between monzogranites and leucogranites, since the former display homogeneous εNd_i values of -8.6 ± 0.2, and the latter more negative ones from -9.9 to -10.5. Indeed, the observed horizontal trend for the monzogranites in the SiO_2 vs. εNd_i diagram diverges from the apparent vertical trend evidenced by the leucogranites (Fig. 6b).

8. Discussion

8.1. Geochemical modelling of granite evolution

Partial melting, fractional crystallization, and magma mixing/assimilation are assumed to be the main petrogenetic processes that may control the geochemical evolution of granitoid suites (e.g. Clemens and Stevens, 2012; Moyen et al., 2021; Nabelek, 2020). Although considering the coeval nature of studied monzogranites and leucogranites, differences observed in whole-rock geochemistry require a separate consideration in regard to their internal differentiation. Nearly identical εNd_i values of studied monzogranite samples preclude mixing processes as the main differentiation-controlling factor, and their homogeneous $^{87}Sr/^{86}Sr_i$ ratios discard also assimilation processes (e.g. Gao et al., 2016; Janoušek and Moyen, 2020; Fig. 6). Only the variance of the monzogranite sample LBA-12 may reflect some local assimilation of more radiogenic materials or mixing processes developed between the monzogranites and leucogranites (limited to the contact areas between them). This is in agreement with the $^{87}Sr/^{86}Sr_i$ vs. εNd_i diagram. They plot out of the regional mixing trend of Variscan igneous rocks, depicting lower $^{87}Sr/^{86}Sr_i$ ratios and a horizontal path, precluding their interpretation as mixed products between regional mantle-derived magmas and strongly peraluminous leucogranite magmas (Fig. 6a).

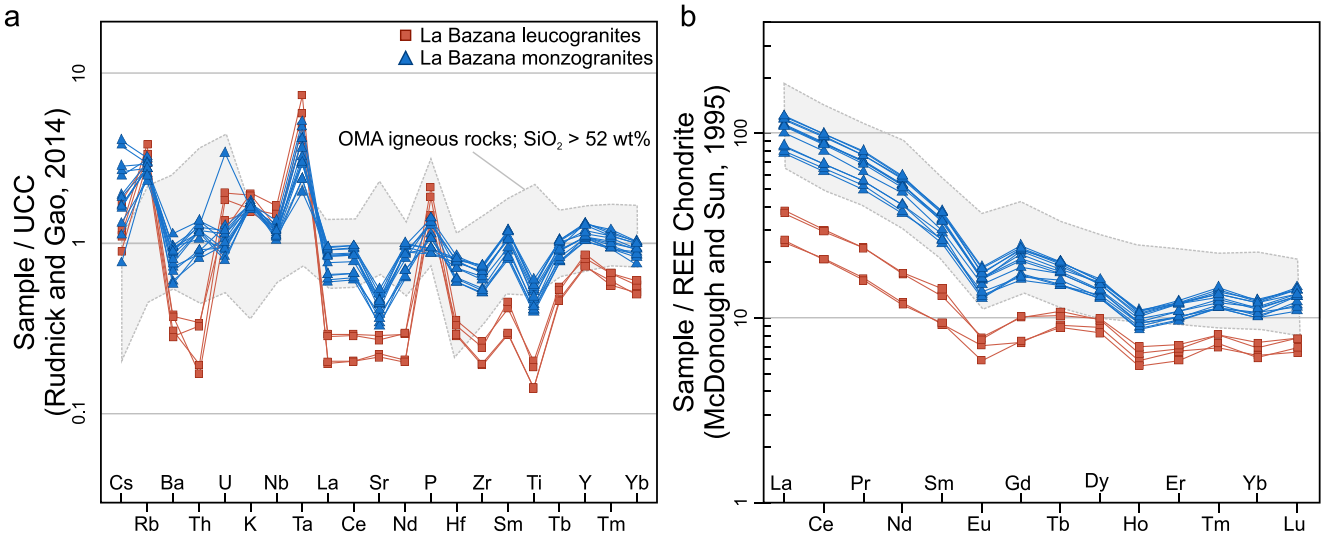

Fig. 5. (a) Whole-rock Upper Continental Crust normalized (UCC) (normalization values from Rudnick and Gao, 2014) multielemental diagram and (b) chondrite normalized (normalization values from McDonough and Sun, 1995) REE diagram of studied monzogranites and leucogranites (compositions of intermediate–acid Variscan igneous rocks from the OMA also drawn).

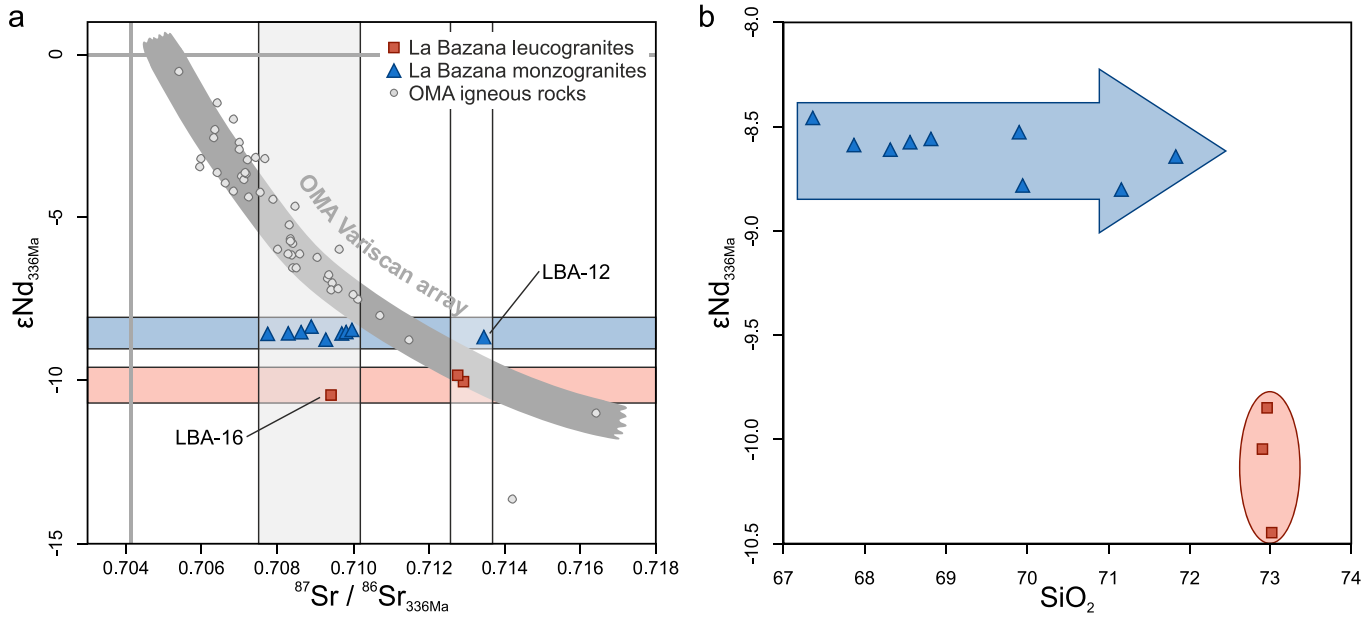

Fig. 6. (a) Whole-rock initial (336 Ma) $^{87}Sr/^{86}Sr$ vs. εNd binary plot for La Bazana monzogranites and leucogranites. The linear array defined by Variscan igneous rocks from the OMA is shown for comparison. This 'OMA Variscan array' would represent a geochemical trend were mantle participation is contended in the generation of granitoids (sensu *lato*) (see Cambeses et al., 2019). Data taken from Cambeses et al., 2015, 2019; Casquet et al., 2001; Sarrionandia, 2006; Tornos et al., 2006). (b) SiO_2 vs. εNd_{336Ma} diagram for La Bazana monzogranites and leucogranites.

The studied monzogranites display well-defined trends in SiO_2 vs. major- and trace-element diagrams (Supplementary Fig. 2), and nearly vertical trends in incompatible vs. compatible plots (e.g. Rb vs. Ba; Nb vs. Sr). These trends suggest dominance of fractional crystallization over partial melting.

The geochemical modelling developed for the studied set of samples supports fractional crystallization as the main controlling mechanism to explain the internal evolution of the studied biotite-bearing monzogranites. For major elements, mass-balance equations and the constrained least-square method were used for reverse modelling (following Janoušek and Moyen, 2020). Considering the less differentiated sample LBA-08 (SiO_2 = 67.37 wt%) as the parental magma and the most siliceous sample LBA-13 (SiO_2 = 71.84 wt%) as the most evolved magma, the geochemical variation of SiO_2, Al_2O_3, FeO^t, MgO, CaO, Na_2O, K_2O, TiO_2, and P_2O_5 can be modelled by ~29% degree of fractional crystallization (FC) of plagioclase (~53%; Ab_{58}) + biotite (~32%; mg# = 0.44), and quartz (~15%), with an acceptable sum of squared residuals (ΣR^2) of 0.973 (numerical results in Supplementary Table 8 and graphic results in Supplementary Fig. 3). According to these results, the generated cumulate would be a tonalite of intermediate composition (SiO_2 = 56.96).

Modelling of trace elements was carried out by the direct method,

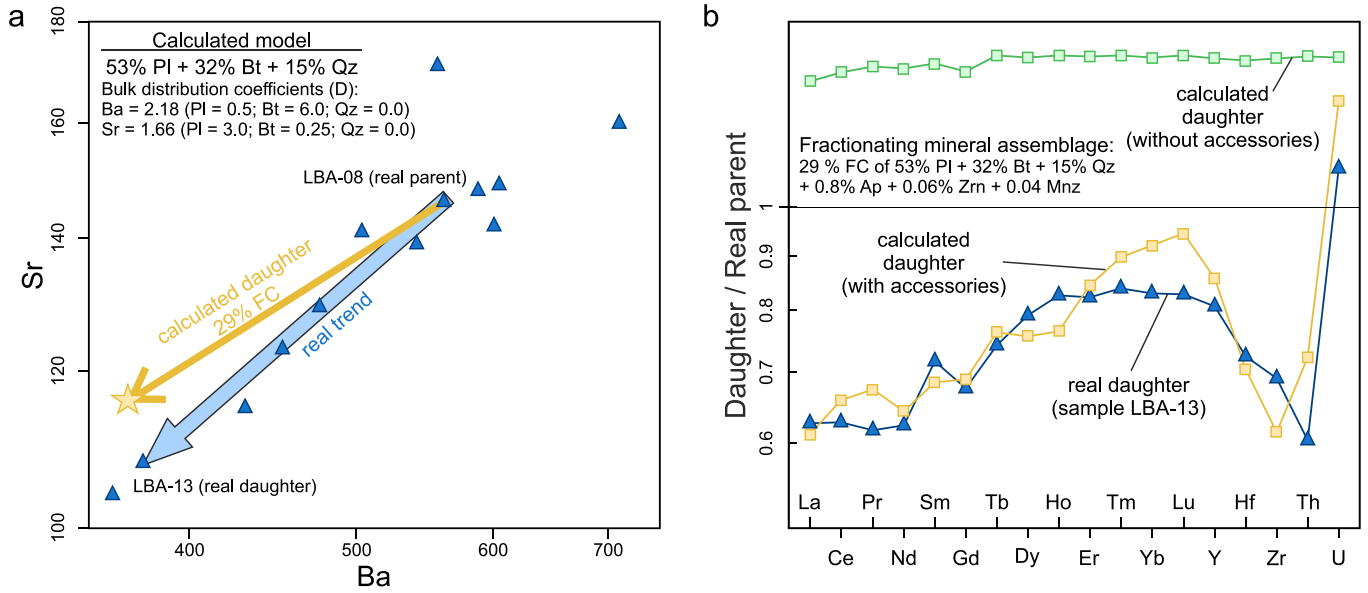

Fig. 7. Graphic results of the performed trace element geochemical modelling for the La Bazana Pluton biotite-bearing monzogranites: (a) Ba-Sr modelling (partition coefficients from Ewart and Griffin, 1994). (b) Key trace-element modelling (daughters have been normalized to the parental LBA-08 sample). The partition coefficients used for the modelling are detailed in Supplementary Table 9 (K_D taken from Bachmann et al., 2005; Errandonea-Martin et al., 2019; Padilla and Gualda, 2016).

based on Rayleigh-type fractional crystallization ($C_L = C_0\ F^{(D-1)}$), where C_L is the calculated 'daughter' or evolved magma, C_0 is the parental magma, F is the amount of melt fraction (1-FC), and D is the bulk distribution coefficient. In the case of trace elements controlled mainly by main rock-forming minerals, Ba and Sr behave as compatible elements, whereas Rb and Cs show a positive correlation with SiO_2. Accordingly, the evolution of Ba and Sr in the biotite-bearing monzogranitic samples was modelled based on the aforementioned fractionating mineral assemblage (Pl + Bt + Qz) obtaining satisfactory results with ~29% FC (Fig. 7a). The modelling of other relevant trace elements, controlled mostly by accessory minerals (such as Th, U, Y, Hf, Zr and REE; e.g. Bea, 1996), was performed to assess the validity of the fractionation model, proving that it is a plausible model considering the composition of the calculated evolved magma (Fig. 7b). The developed modelling (partition coefficients in Supplementary Table 9) involves a coherent proportion of Ap (0.80%) + Zr (0.06%) + Mnz (0.04%) in the fractionating mineral assemblage (Fig. 7b).

On the other hand, the studied leucogranites do not reflect any evolutionary trend, with nearly similar SiO_2 contents in all of them. The studied samples do not align with the set of biotite-bearing monzogranites in the SiO_2 vs. major-element binary diagrams, especially in the case of TiO_2, CaO, K_2O and P_2O_5. The behavior is similar to most analyzed trace elements, with remarkable gaps in the case of Cs, Th, Y, and REE. Accordingly, the studied leucogranites could represent discrete magma pulses derived from different degrees of partial melting rather than constitute the most evolved terms of a fractional crystallization process.

8.2. Zircon- and whole-rock-based geothermometry

Estimation of melting and crystallization temperatures is fundamental in granite petrogenesis, and zircon appears to be a key mineral in its assessment (Bea et al., 2021; Miller et al., 2003; Siégel et al., 2018). The Ti-in-zircon geothermometer (Ferry and Watson, 2007) and whole-rock zircon saturation geothermometer (Watson and Harrison, 1983) have been largely used and tested over the years (e.g. Schiller and Finger, 2019; Siégel et al., 2018). Temperatures derived from Ti contents in zircon crystals from La Bazana monzogranites were calculated based on the calibrations of Ferry and Watson (2007) and the corrections of Schiller and Finger (2019). Assuming typical values in granites of 0.5 and 1.0 for the respective a_{TiO2} and a_{SiO2} parameters (Schiller and Finger, 2019), a correction of +70 °C was considered for the resultant temperatures. Accordingly, a range of temperatures from 731 to 844 °C was obtained, with 80% of results varying from ~730 to 780 °C. The high whole-rock silica contents ($SiO_2 > 67$ wt%) and the compatible behavior of Zr (negative correlation in whole-rock SiO_2 vs. Zr) in the monzogranites from La Bazana point to a zircon saturated melt. The inherited domains in the studied zircon would imply the increasing of the zircon saturation temperatures in ~25 °C for the less evolved monzogranite samples (following Siégel et al., 2018). The obtained results for these samples vary in the range of 740–750 °C, in line with the obtained Ti-in-zircon temperatures. As complementary, monazite and apatite saturation temperatures were also calculated for the studied biotite-bearing monzogranites. Monazite saturation temperatures after Montel (1993) yield temperatures between 760 and 780 °C for the less evolved monzogranites and apatite saturation temperatures based on Pichavant et al. (1992) give too-low temperatures and were discarded. We thus propose that the less evolved monzogranites from La Bazana crystallized in the range of 730–780 °C. In the case of leucogranites zircon and monazite saturation temperatures should be taken with caution (see Nabelek, 2020), although the overall range of 670–725 °C obtained for the studied two-mica leucogranites seems reasonable.

All in all, the temperature estimations give values mainly under 800 °C for the biotite-bearing monzogranites and under 720 °C for the two-mica leucogranites. According to Miller et al. (2003) and Bea et al. (2021), zircon saturation temperatures below 800 °C, together with the relatively high amount of zircon inheritances, imply that the studied monzogranites are 'cold' and 'wet' granites. Based on Bea et al. (2021), melting of fertile peraluminous greywackes and/or orthogneisses, with 3–5 wt% of H_2O at pressures of 4–6 kbar, could have generated the parental magmas of studied monzogranites. Considering that according to Galadí-Enríquez et al. (2003), the La Bazana Pluton represents a small allochthonous intrusive originated at the middle crust and emplaced at 2–3 kbar, the mentioned scenario is feasible. On the contrary, zircon saturation temperatures of < 700 °C and mid-crustal pressure conditions could indicate melting of water-rich sources ($H_2O \geq 8$ wt%) for the generation of the studied two-mica leucogranites.

8.3. Assessment of mantle role in the genesis of weakly peraluminous monzogranite magmas in La Bazana

La Bazana Pluton intruded into the upper-continental crust while an intra-orogenic transcurrent setting governed the area. This led to local transtension that favored the upwelling of the asthenospheric mantle and melting of the lithospheric mantle at ca. 330–345 Ma (e.g.Cambeses et al., 2019; Rodríguez et al., 2022). During this period, voluminous I-type magnesian, calcic-alkalic to alkali-calcic, and metaluminous granitoids that form a cafemic association emplaced simultaneously to the La Bazana Pluton in the OMA. Their origin has been proposed to result from the hybridization of mantle-derived magmas with crustal melts, pointing to significant mantle participation in the area. This participation was not only as a heat supply, but also as magma injections to generate new continental crust (e.g. Cambeses et al., 2015, 2019; Sarrionandia, 2006). Similarly, in the Évora massif to the west of the OMZ, the first Variscan magmatic episode described by Rodríguez et al. (2022) is related to crustal melting processes associated with the D_2 ductile extensional deformation. These 'calc-alkaline' rocks, interpreted as evolved from a parental andesitic (dioritic) magma, are contemporaneous to the intrusion of the La Bazana Pluton. The estimated emplacement condition, either for the contemporaneous Évora granitoids or those from the OMA in central Ossa–Morena, is ~3 kbar (Cambeses et al., 2019; Rodríguez et al., 2022), which is in agreement with the emplacement pressure conditions of La Bazana estimated here. Indeed, major- and trace-element compositions of the studied biotite-bearing monzogranites are comparable to the most evolved terms of the 'calc-alkaline' granitoid suites from the OMA (Figs. 4 and 5). According to Moyen et al. (2021), when comparing the two main paradigms of granitoid formation (mantle-derived basaltic magma fractionation vs. crustal melting) volcanic rocks are distinctive of the former. Therefore, the widespread volcanic record of the OMZ, coeval with the magmatism here studied, also suggests a significant mantle involvement in the region.

Considering the above, most of peraluminous terms that form the mentioned associations (gabbro–diorite–tonalite–granodiorite–granite) in Évora and the OMA would broadly represent the differentiation of an I-type, metaluminous, mantle-derived magma. Despite the relatively high A/CNK values in some cases, their close relationship with less evolved/more mafic terms, as well as the absence of inherited zircon, points to an evolved mantle-derived infracrustal I-type magmas (Cambeses et al., 2015; Pereira et al., 2015). In this context, the parental magmas that gave rise to La Bazana monzogranites, generated at mid-crustal levels, are spatially related to the abundant mantle-derived magmas that intruded contemporaneously into the same levels. Based on that, the origin of peraluminous granitoids from La Bazana could be considered equivalent to those from Évora and the OMA. However, their Sr-Nd isotope geochemistry and zircon inheritances rather discard this hypothesis. As stated in Section 8.1, 'crustal-like' homogeneous whole-rock εNd_i isotopes and the fractional crystallization modelling discard the participation of primary mantle-derived magmas as end-members of a theoretical mixing process to explain the geochemical evolution in La Bazana (Figs. 6 and 7). Therefore, we reckon that, although mantle-derived melts may have probably behaved as a source of heat, they did not contribute to the parental monzogranitic magmas of the La

Bazana Pluton. The main outcome is that crustal melting within the region was not limited to the generation of localized melts leading to the hybridization of I-type magmas, but it expanded sufficiently to give rise to allochthonous plutons.

8.4. Deciphering sources of weakly-peraluminous monzogranite magmas

Zircon inheritances provide invaluable information about the melted protoliths as remnants of the source rocks in the newly generated granite magmas (e.g. Bea et al., 2021; Miller et al., 2003). For the case studied here, the main zircon generating tectonomagmatic events would have been the lower Paleozoic rifting (e.g. Chichorro et al., 2008; Pereira et al., 2012; Sánchez-García et al., 2008; Sarrionandia et al., 2012; Solá, 2007; Solá et al., 2008), and the previous Cadomian subduction-related processes (Fernández-Suárez et al., 2002; Henriques et al., 2015; Ordoñez-Casado, 1998; Pereira et al., 2011, 2012; Sánchez-Lorda et al., 2014, 2016; Sarrionandia et al., 2020). As shown in Fig. 8, zircon inheritances in La Bazana monzogranites coincide overall with the maximum $^{206}Pb/^{238}U$ age peaks of both tectonomagmatic events. This overlapping, together with the number of zircon crystals showing inherited domains, supports the crustal melting instead of fractionation of an intermediate (mantle-derived) 'calc-alkaline' magma (in the sense of Castro, 2020; Gómez-Frutos et al., 2023). This is in agreement with the calculated zircon saturation temperatures, which imply a main melting process of metagreywackes and/or orthogneisses with a metapelitic component (+ H_2O). Moreover, studied compositions of monzogranites plot within the field of melts derived from metagreywackes in the molar CaO / (MgO + FeO^t) vs. Al_2O_3 / (MgO + FeO^t) diagram and clay-poor sources in the Rb/Sr vs. Rb/Ba diagram (Fig. 9; after Gerdes et al. (2002) and Sylvester (1998), respectively). CaO/Na_2O ratios (> 0.30), as well as their low Al_2O_3 / (FeO^t + MgO + TiO_2) (wt%) ratios (< 7), also point to psammite−/greywacke−/orthogneiss-derived sources. It is suggested that several 'Cadomian-related' zircon inheritances could already be unmelted remnants within the subsequent rift-related magmatic rocks (whose protoliths are related to the previous crustal basement) (e.g. Sánchez-García et al., 2008; Solá et al., 2008).

In addition to the above, whole-rock Sr-Nd isotope compositions of regional crustal rocks allow tracking the possible sources and discriminating primary rocks from the more evolved ones (older/reworked). Initial εNd values (age-corrected to 336 Ma) of the La Bazana biotite-bearing monzogranites display compositions in the range of the Cambro–Ordovician rift-related felsic magmatic rocks (εNd_{336} = 0 to −10; Sánchez-García et al., 2010), felsic metaigneous rocks from the older Cadomian Sardoal Complex (εNd_{336} = −6 to −11; Henriques et al., 2015) and Cadomian metapelites and metagreywackes from the Serie Negra Group (εNd_{336} < −5; Díez Fernandez et al., 2017; Fuenlabrada et al., 2021; Rojo-Pérez et al., 2021; Fig. 10). Melting of such protoliths, felsic orthogneisses and/or metagreywackes (± metapelites?), is in line with the estimated P, T and H_2O conditions, and whole-rock geochemistry for the studied La Bazana monzogranites.

On the contrary, the studied leucogranites display high molar Al_2O_3 / (MgO + FeO^t) and low CaO / (MgO + FeO^t) ratios, as well as strongly peraluminous compositions (A/CNK values up to 1.53). Low-TiO_2 contents of ~0.11 wt%, FeO^t + MgO values of ~1.6 wt%, Ca/Na (molar) ratios of ~0.12, as well as high Rb/Ba and Rb/Sr ratios (Fig. 9) resemble geochemical features of collisional leucogranites and experimental melts obtained from metapelitic and quartz-feldspathic rocks (Nabelek, 2020; Sylvester, 1998). According to these authors, low Sr contents in leucogranites, like the studied herein, could derive from the preferential consumption of albitic plagioclase over the anorthite component during melting (Sr substitutes Ca). Similarly, low-Ba contents would indicate incomplete consumption of feldspars (Ba remains in K-feldspar) and the negligible role of the biotite in the process, supported by the low-Mg, -Fe and -Ti contents. Likewise, low-Th, -Zr and -REE contents in the studied leucogranites may be attributed to the preservation of monazite and zircon inclusions enclosed in residual biotite. The incomplete melting of feldspars and the (near) absence of biotite dehydration reactions point to a vapour-absent melting by muscovite dehydration of pelitic sedimentary rocks (e.g. Nabelek, 2020). Calculated zircon saturation temperatures for the here studied leucogranites (< 700 °C) suggest a 'low-temperature' environment in the magma source region. This supports muscovite dehydration melting as the main mechanism for leucogranite generation instead of muscovite + biotite dehydration melting (e.g. Nabelek, 2020). Significantly negative εNd_i values of about −10 obtained for the studied leucogranites coincide with εNd_i values of the metasedimentary sequences of the Serie Negra Group (Fig. 10), pointing

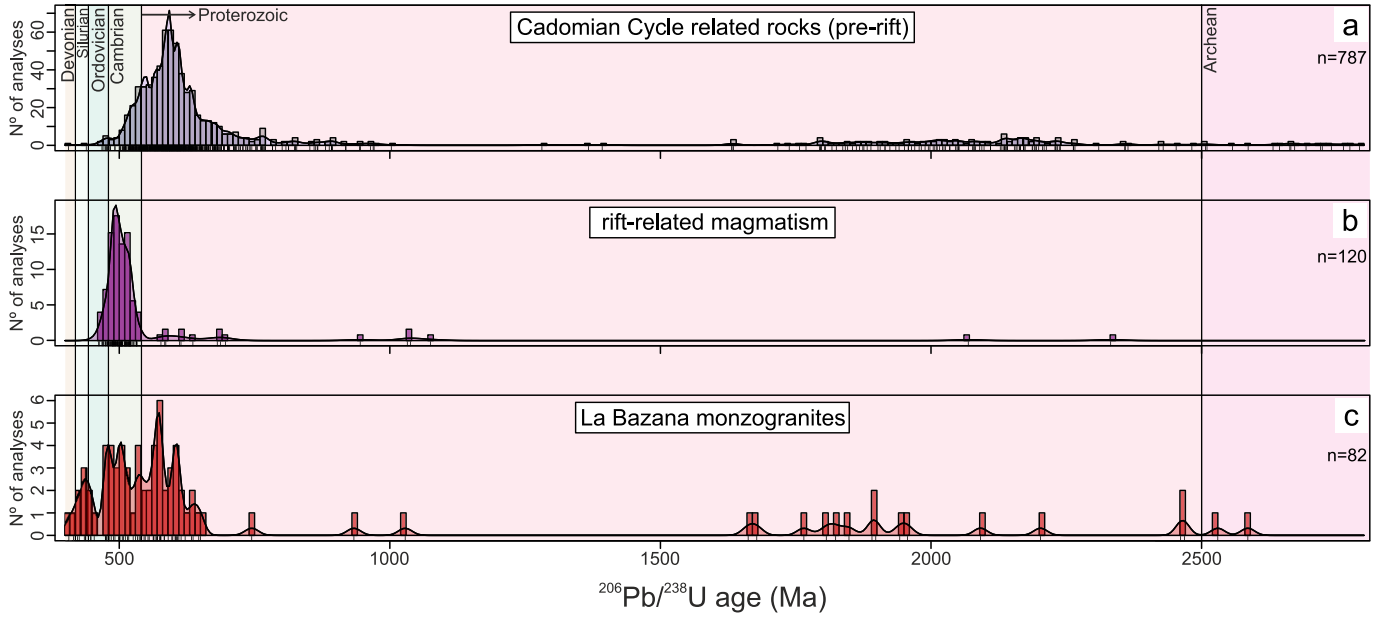

Fig. 8. Histograms of $^{206}Pb/^{238}U$ ages obtained from: (a) rocks ascribed to the Cadomian orogenic cycle, (b) subsequent rift-related magmatism, and (c) inherited zircon cores identified in La Bazana monzogranites. Data related to the Cadomian cycle taken from Fernández-Suárez et al. (2002), Henriques et al. (2015), Ordoñez-Casado (1998), Pereira et al. (2011, 2012), Sánchez-Lorda et al. (2014, 2016), and Sarrionandia et al. (2020), and data about the rift-related magmatism from Chichorro et al. (2008), Pereira et al. (2012), Sánchez-García et al. (2008), Solá (2007), and Solá et al. (2008).

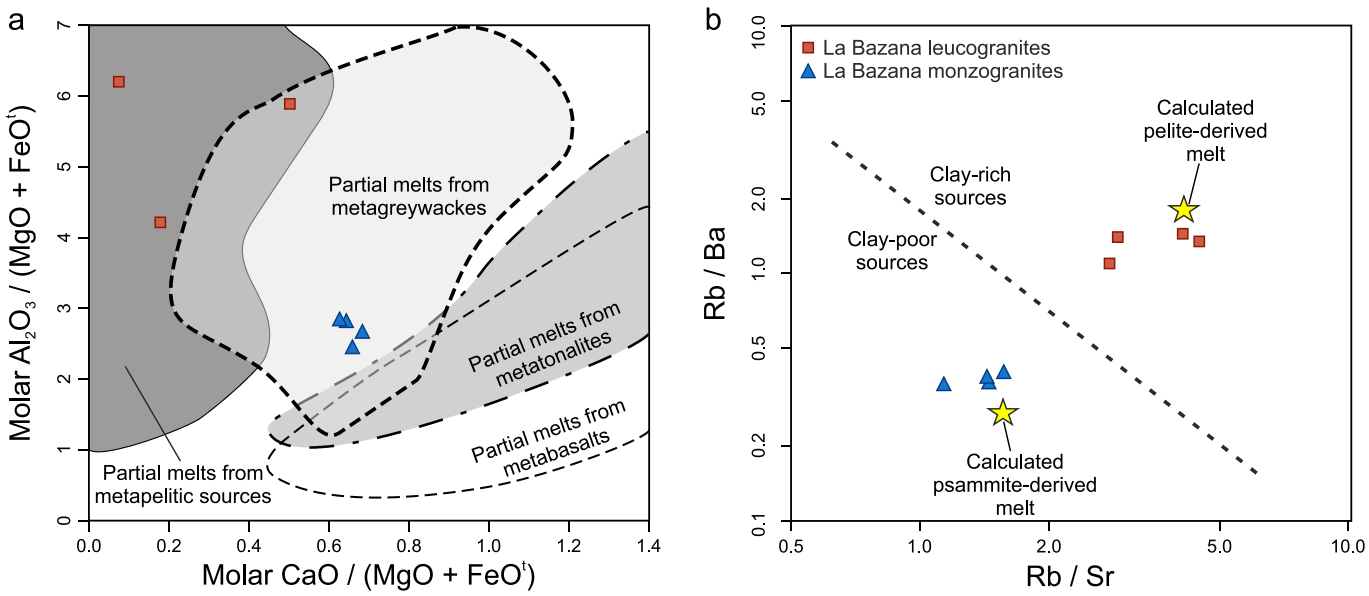

Fig. 9. Granite source discrimination diagrams for La Bazana monzogranites and leucogranites: (a) Molar CaO/(MgO + FeO^t) vs. Al_2O_3/(MgO + FeO^t) diagram based on Gerdes et al. (2002) with fields of experimental melts derived from partial melting of metabasalts, metatonalites, metagreywackes and metapelites. (b) Clay-poor and clay-rich source discrimination Rb/Sr vs. Rb/Ba diagram (Sylvester, 1998). In the case of monzogranites only the less-evolved samples were projected.

to the melting of Ca-poor metapelites within it as the origin of the melts (probably from the so-called 'Montemolín Succession') (e.g. Cambeses et al., 2017, and references therein).

8.5. S- and I-type granite magmatism in intra-orogenic transcurrent domains

The unequivocal contribution of rift-related felsic Cambro–Ordovician (meta-) igneous rocks as protolith of the studied biotite-bearing monzogranites, revealed by the zircon inheritances, suggests their classification as I-type (igneous). Nevertheless, since it cannot be determined the percentage of input of metasediments of the Serie Negra Group (major- and trace-elements match either orthogneiss- and greywacke-derived melts), the high amount of zircon inheritances may also support a partial derivation from fertile metasedimentary sources (e.g. Bea et al., 2021). This would strengthen the consideration of the studied monzogranites as S-type (sedimentary), which leads to a dichotomy between S-type and I-type signatures for La Bazana monzogranites. It should be noted that the previously mentioned mantle-derived magmas, simultaneously intruded into the OMZ at mid-crustal levels, could have favored also local melting of mid-crustal metaigneous/metasedimentary rocks, providing enough heat supply (plus H_2O?) to cause reworking of the continental crust. Thereby, the biotite-bearing monzogranites studied could also fit with the 'secondary' I-type granites of Castro (2020), with mantle-derived magmas as water donors and thermal agents that lead to the melting of continental crust. However, such 'secondary' I-type magmas are related to lower-crustal melting (implying temperatures of $>$ 900 °C; Castro, 2020), where zircon inheritances can easily dissolve during anatexis and formation of the new granodioritic melt (e.g. Bea et al., 2021; Miller et al., 2003). With the estimated lower melting/initial-crystallization temperatures of ~730–780 °C and H_2O contents of 3–5 wt% (together with high zircon inheritances) a mid-crustal origin seems more suitable for the La Bazana monzogranites. As a consequence, regardless of whether the required H_2O derives from an unfertile pelitic (water-rich) source or from mantle-derived magmas, melting of felsic metaigneous + quartz-feldspathic metasedimentary crustal rocks seems the most feasible alternative for the generation of the studied biotite-bearing monzogranites. Given those source rocks and estimated P-T conditions, the studied monzogranites can be defined as 'cold' or 'low-temperature' granites (as described by Miller et al. (2003) and Chappell et al. (2004), respectively), more precisely as 'wet' granitoids (Bea et al., 2021), and S-type, but as 'supracrustal' rather than exclusively sediment-derived.

Despite that there is little doubt about the consideration of the strongly peraluminous leucogranites from La Bazana as S-type, the initially ambiguous (S-/I-type) character of the studied biotite-bearing monzogranites reinforces the idea of the complex granitoid magmatism in transcurrent settings. In these environments, lithospheric shear zones may act not only as channels that enable the upward transfer and emplacement of magmas from mantle depths to the upper crust but also as crustal melting-promoting mechanisms. Since melting of diverse sources and magma ascent occur localized in the shear zones, these structures favor the interaction between magmas of contrasting nature. Leaving aside local transpressional areas, transtensional zones could be analogous to post-collisional settings in terms of granitoid generation. In these environments metaluminous to weakly peraluminous associations of I-type amphibole-bearing and potassic calc-alkaline granitoids of infracrustal origin are coeval with cordierite- and/or muscovite-bearing strongly peraluminous granitoids of supracrustal origin (Barbarin, 1999; Moyen et al., 2017; Sylvester, 1998). Compared with arc magmatism, the input of new mantle-derived juvenile magmas in the continental crust is reduced in post-collisional settings, but their high probability of preservation implies that this magmatism contributes significantly to the generation of new continental crust (Gómez-Frutos et al., 2023; Jacob et al., 2021; Moyen et al., 2017). This could be the case for most of OMZ 'calc-alkaline' granitoids generated in an extensional/transtensional setting. Nonetheless, what the present study reveals is that coeval crustal reworking in these intra-orogenic transcurrent and mantle-dominated systems may be greater than expected.

9. Conclusions

Magnesian, alkali-calcic, and weakly- to strongly-peraluminous biotite-bearing monzogranites and magnesian-ferroan, alkali-calcic, and strongly peraluminous two-mica leucogranites constitute the intrusive assemblage of the La Bazana Pluton. These granites crystallized at 336.3 ± 0.7 Ma (U-Pb in zircon) in an intra-orogenic transtensional setting where mantle-derived magmas were dominant. Whole-rock CaO/Na_2O ratios of $>$ 0.30 and Al_2O_3 / (FeO^t + MgO + TiO_2) values of $<$ 7 suggest a quartz-feldspathic source for the monzogranites that,

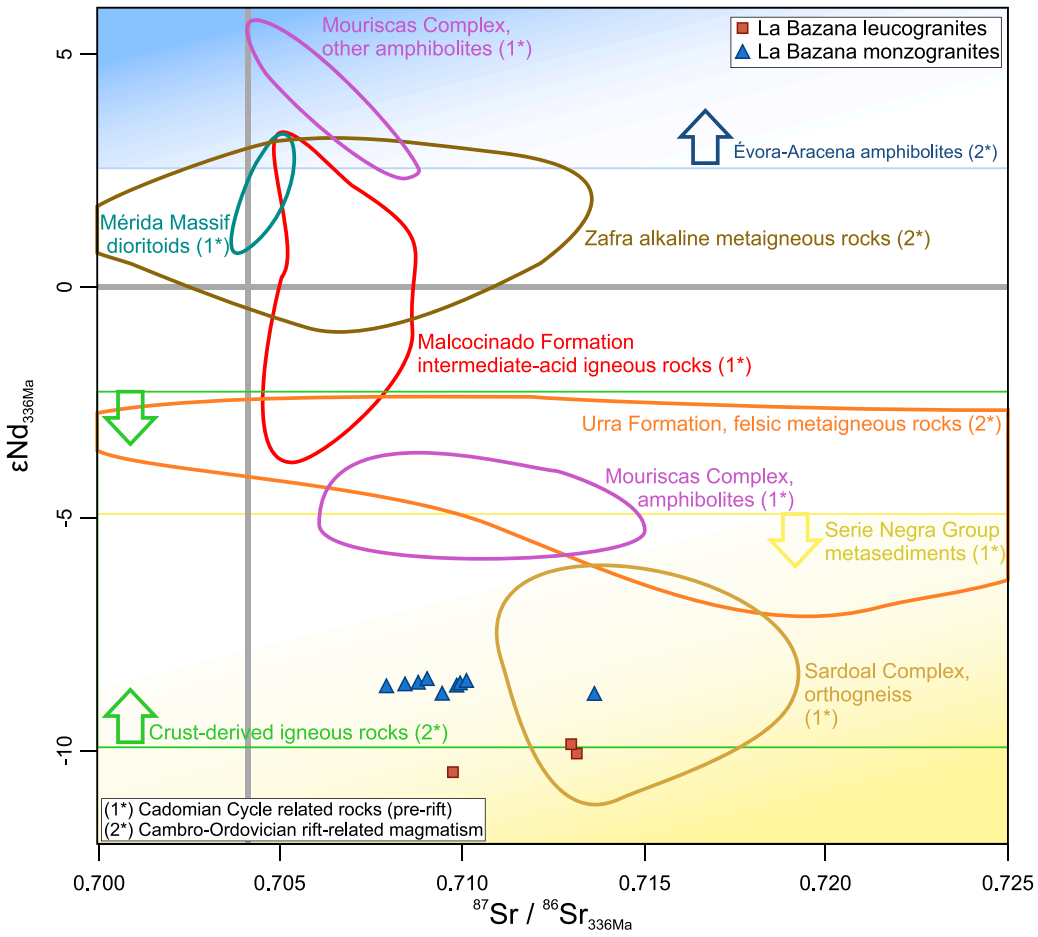

Fig. 10. Whole-rock $^{87}Sr/^{86}Sr$ vs. εNd binary plot for La Bazana monzogranites and leucogranites that includes potential source rocks (isotopic ratios recalculated to 336 Ma). The bluish shading on the upper left side and the yellowish shading on the lower right side represent mantle-like and crustal-like (respectively) isotopic ratios of probable regional source rocks. In the case of Évora-Aracena amphibolites and crust-derived igneous rocks only Nd isotopic data were found in the literature. Data for the drawn fields were taken from Bandrés et al. (2004) (Mérida Massif dioritoids), Chichorro et al. (2008) (Évora-Aracena amphibolites), Solá et al. (2008) (Urra Formation felsic metaigneous rocks), Díez Fernandez et al. (2017), Fuenlabrada et al. (2021), López-Guijarro et al. (2008), Rojo-Pérez et al. (2021) (Serie Negra Group or equivalent), Sánchez-García et al. (2010) (crust-derived Cambro-Ordovician igneous rocks), Sarrionandia et al. (2012) (Zafra alkaline metaigneous rocks), Henriques et al. (2015) (Sardoal Complex orthogneisses and Mouriscas Complex amphibolites) and Sarrionandia et al. (2020) (Malcocinado Formation intermediate-acid rocks).

coupled with both zircon inheritances (related to the Cadomian and subsequent rifting tectonomagmatic events) and whole-rock εNd_i values (-8.6 ± 0.2), reinforce a heterogeneous source area composed by Late Ediacaran – Upper Cambrian metagreywackes and felsic metaigneous rocks. By contrast, their low CaO/Na_2O (< 0.21), high Rb/Ba (~1.3) and Rb/Sr (~3.5) ratios, together with negative εNd_i values from −9.9 to −10.5, indicate that leucogranite magmas mainly derived from melting of Ediacaran Ca-poor metapelites. Melting of such crustal lithologies occurred at mid-crustal levels and was likely prompted by asthenospheric upwelling, intrusion of coeval mantle-derived magmas and shear heating. Resulting granitoid magmas intruded a posteriori into the upper crust at 2–3 kbar, with estimated crystallization temperatures of 730–780 °C for the monzogranites and 670–725 °C for the leucogranites. The geochemical modelling developed for the biotite-bearing monzogranites supports fractional crystallization as the main controlling mechanism to explain their internal geochemical evolution, with 29% fractionation of Pl (~53%) + Bt (~32%) + Qz (~15%) + Ap (0.80%) + Zrn (0.06%) + Mnz (0.04%). On the contrary, studied leucogranites seem not to be cogenetic with the monzogranites and would represent discrete magma pulses derived from different degrees of partial melting of metapelites. Rather than evolved terms of a mantle-derived magmatic association, the studied weakly- to strongly-peraluminous biotite-bearing monzogranites and two-mica leucogranites depict a crustal reworking process presumably triggered by a mantle-related thermal anomaly. This contribution strengthens the conception that in intra-orogenic transcurrent regimes diverse granitoid-generating mechanisms may act concurrently, making their classification complex, and that crustal melting in such environments may be broader than previously assumed.

Declaration of competing interest

The authors declare that they have no known competing financial interests or personal relationships that could have appeared to influence the work reported in this paper.

Acknowledgements

Financial support was provided by the Spanish Ministry of Economy, Industry and Competitiveness and the European Regional Development Fund (MINECO/FEDER CGL2015-63530-P), and by the University of the Basque Country UPV/EHU (GIU20/010; GIU21/008). The authors are grateful to the Co-Editor-in-Chief Dr. Greg Shellnutt for his editorial handling, as well as to Dr. Peng Gao and an anonymous reviewer for providing constructive comments. The authors would like to thank for the technical and human support provided by SGIker of the UPV/EHU

and European funding (EDRF and ESF). Useful comments on a previous version of the manuscript made by two anonymous reviewers are also acknowledged.

Appendix A. Supplementary data

Supplementary data to this article can be found online at https://doi.org/10.1016/j.lithos.2024.107555.

References

Ábalos, B., Gil Ibarguchi, J.I., Eguiluz, L., 1991. Cadomian subduction, collision and Variscan transpression in the Badajoz-Cordoba Shear Belt, Southwest Spain. Tectonophysics 199 (1), 51–72. https://doi.org/10.1016/0040-1951(91)90118-C.

Ábalos, B., Puelles, P., Gil Ibarguchi, J.I., 2022. Polyphase tectonic reworking of serpentinites and chlorite-tremolite-talc rocks (SW Spain) from the subduction forearc to intracontinental emplacement. J. Metamorph. Geol. 1–33 https://doi.org/10.1111/jmg.12704.

Bachmann, O., Dungan, M.A., Bussy, F., 2005. Insights into shallow magmatic processes in large silicic magma bodies: the trace element record in the fish Canyon magma body, Colorado. Contrib. Mineral. Petrol. 149 (3), 338–349. https://doi.org/10.1007/s00410-005-0653-z.

Bandrés, A., Eguíluz, L., Pin, C., Paquette, J.L., Ordoñez, B., Le Fèvre, B., Ortega, L.A., Gil Ibarguchi, J.I., 2004. The northern Ossa-Morena Cadomian batholith (Iberian Massif): magmatic arc origin and early evolution. Int. J. Earth Sci. 93 (5), 860–885. https://doi.org/10.1007/s00531-004-0423-6.

Barbarin, B., 1996. Genesis of the two main types of peraluminous granitoids. Geology 24 (4), 295–298. https://doi.org/10.1130/0091-7613(1996)024<0295:GOTTMT>2.3.CO;2.

Barbarin, B., 1999. A review of the relationships between granitoid types, their origins and their geodynamic environments. Lithos 46 (3), 605–626. https://doi.org/10.1016/S0024-4937(98)00085-1.

Bea, F., 1996. Residence of REE, Y, Th and U in granites and crustal protoliths; implications for the chemistry of crustal melts. J. Petrol. 37 (3), 521–552. https://doi.org/10.1093/petrology/37.3.521.

Bea, F., Fershtater, G., Corretgé, L.G., 1992. The geochemistry of phosphorus in granite rocks and the effect of aluminium. Lithos 29 (1–2), 43–56. https://doi.org/10.1016/0024-4937(92)90033-U.

Bea, F., Morales, I., Molina, J.F., Montero, P., Cambeses, A., 2021. Zircon stability grids in crustal partial melts: implications for zircon inheritance. Contrib. Mineral. Petrol. 176, 18. https://doi.org/10.1007/s00410-021-01772-x.

Bonin, B., Janoušek, V., Moyen, J.-F., 2020. Chemical variation, modal composition and classification of granitoids. Geol. Soc. Lond. Spec. Publ. 491, 9–51. https://doi.org/10.1144/SP491-2019-138.

Cambeses, A., Scarrow, J.H., Montero, P., Molina, J.F., Moreno, J.A., 2015. SHRIMP U–Pb zircon dating of the Valencia del Ventoso plutonic complex, Ossa-Morena Zone, SW Iberia: Early Carboniferous intra-orogenic extension-related 'calc-alkaline' magmatism. Gondwana Res. 28 (2), 735–756. https://doi.org/10.1016/j.gr.2014.05.013.

Cambeses, A., Scarrow, J.H., Montero, P., Lázaro, C., Bea, F., 2017. Palaeogeography and crustal evolution of the Ossa–Morena Zone, southwest Iberia, and the North Gondwana margin during the Cambro-Ordovician: a review of isotopic evidence. Int. Geol. Rev. 59 (1), 94–130. https://doi.org/10.1080/00206814.2016.1219279.

Cambeses, A., Montero, P., Molina, J.F., Hyppolito, T., Bea, F., 2019. Constraints of mantle and crustal sources and interaction during orogenesis: a zircon SHRIMP U-Th-Pb and O isotope study of the 'calc-alkaline' Brovales pluton, Ossa-Morena Zone, Iberian Variscan Belt. Lithos 324–325, 661–683. https://doi.org/10.1016/j.lithos.2018.11.037.

Casquet, C., Galindo, C., Tornos, F., Velasco, F., Canales, A., 2001. The Aguablanca Cu–Ni ore deposit (Extremadura, Spain), a case of synorogenic orthomagmatic mineralization: age and isotope composition of magmas (Sr, Nd) and ore (S). Ore Geol. Rev. 18 (3–4), 237–250. https://doi.org/10.1016/S0169-1368(01)00033-6.

Castro, A., 2020. The dual origin of I-type granites: the contribution from experiments. Geol. Soc. Lond. Spec. Publ. 491, 101–145. https://doi.org/10.1144/SP491-2018-110.

Castro, A., Rodríguez, C., Gutiérrez-Alonso, G., de la Rosa, J.D., 2023. A post-collisional batholith from Southern Iberia rooted in the Earth's mantle: Los Pedroches batholith. Lithos 454–455, 107245. https://doi.org/10.1016/j.lithos.2023.107245.

Chappell, B.W., White, A.J.R., 1992. I- and S-type granites in the Lachlan Fold Belt. Trans. R. Soc. Edinb. Earth Sci. 83 (1–2), 1–26. https://doi.org/10.1017/S0263593300007720.

Chappell, B.W., White, A.J.R., Williams, I.S., Wyborn, D., 2004. Low- and high-temperature granites. Trans. R. Soc. Edinb. Earth Sci. 95 (1–2), 125–140. https://doi.org/10.1017/S0263593300000973.

Chappell, B.W., Bryant, C.J., Wyborn, D., 2012. Peraluminous I-type granites. Lithos 153, 142–153. https://doi.org/10.1016/j.lithos.2012.07.008.

Chichorro, M., Pereira, M.F., Díaz-Azpiroz, M., Williams, I.S., Fernández, C., Pin, C., Silva, J.B., 2008. Cambrian ensialic rift-related magmatism in the Ossa-Morena Zone (Évora–Aracena metamorphic belt, SW Iberian Massif): Sm–Nd isotopes and SHRIMP zircon U–Th–Pb geochronology. Tectonophysics 461 (1–4), 91–113. https://doi.org/10.1016/j.tecto.2008.01.008.

Clemens, J.D., Stevens, G., 2012. What controls chemical variation in granitic magmas? Lithos 134–135, 317–329. https://doi.org/10.1016/j.lithos.2012.01.001.

Clemens, J.D., Stevens, G., Farina, F., 2011. The enigmatic sources of I-type granites: the peritectic connexion. Lithos 126 (3–4), 174–181. https://doi.org/10.1016/j.lithos.2011.07.004.

Debon, F., Le Fort, P., 1983. A chemical–mineralogical classification of common plutonic rocks and associations. Trans. R. Soc. Edinb. Earth Sci. 73, 135–149. https://doi.org/10.1017/S0263593300010117.

Díez Fernández, R., Pereira, M.F., Foster, D.A., 2014. Peralkaline and alkaline magmatism of the Ossa-Morena zone (SW Iberia): age, source, and implications for the Paleozoic evolution of Gondwanan lithosphere. Lithosphere 7 (1), 73–90. https://doi.org/10.1130/L379.1.

Díez Fernandez, R., Fuenlabrada, J.M., Chichorro, M., Pereira, M.F., Sánchez-Martínez, S., Silva, J.B., Arenas, R., 2017. Geochemistry and tectonostratigraphy of the basal allochthonous units of SW Iberia (Évora Massif, Portugal): keys to the reconstruction of pre-Pangean paleogeography in southern Europe. Lithos 268–271, 285–301. https://doi.org/10.1016/j.lithos.2016.10.031.

Eguíluz, L., Gil Ibarguchi, J.I., Ábalos, B., Apraiz, A., 2000. Superposed Hercynian and Cadomian orogenic cycles in the Ossa-Morena zone and related areas of the Iberian Massif. Geol. Soc. Am. Bull. 112 (9), 1398–1413. https://doi.org/10.1130/0016-7606(2000)112<1398:SHACOC>2.0.CO;2.

Errandonea-Martin, J., Sarrionandia, F., Janoušek, V., Carracedo-Sánchez, M., Gil Ibarguchi, J.I., 2019. Origin of cordierite-bearing monzogranites from the southern Central Iberian Zone – inferences from the zoned Sierra Bermeja Pluton (Extremadura, Spain). Lithos 342–343, 440–462. https://doi.org/10.1016/j.lithos.2019.06.009.

Ewart, A., Griffin, W.L., 1994. Application of proton-microprobe data to trace-element partitioning in volcanic rocks. Chem. Geol. 117 (1–4), 251–284. https://doi.org/10.1016/0009-2541(94)90131-7.

Fernández Carrasco, J., Coullaut Saenz de Sicilia, J.L., Aguilar Tomás, M.J., 1981. Sheet Number 875 (Jerez de los Caballeros) of the Geological Map of Spain at Scale 1: 50.000 (MAGNA 50, 2nd series). Geological Survey of Spain (IGME), Madrid retrieved from. http://info.igme.es/cartografiadigital/geologica/Magna50Hoja.aspx?intranet=false&id=875.

Fernández-Suárez, J., Gutiérrez Alonso, G., Jeffries, T.E., 2002. The importance of along-margin terrane transport in northern Gondwana: insights from detrital zircon parentage in Neoproterozoic rocks from Iberia and Brittany. Earth Planet. Sci. Lett. 204 (1–2), 75–88. https://doi.org/10.1016/S0012-821X(02)00963-9.

Ferry, J.M., Watson, E.B., 2007. New thermodynamic models and revised calibrations for the Ti-in-zircon and Zr-in-rutile thermometers. Contrib. Mineral. Petrol. 154, 429–437. https://doi.org/10.1007/s00410-007-0201-0.

Flecha, I., Carbonell, R., Zeyen, H., Martí, D., Palomeras, I., Simancas, F., Pérez-Estaún, A., 2006. Imaging granitic plutons along the IBERSEIS profile. Tectonophysics 420 (1–2), 37–47. https://doi.org/10.1016/j.tecto.2006.01.019.

Frost, B.R., Barnes, C.G., Collins, W.J., Arculus, R.J., Ellis, D.J., Frost, C.D., 2001. A geochemical classification for granitic rocks. J. Petrol. 42 (11), 2033–2048. https://doi.org/10.1093/petrology/42.11.2033.

Fuenlabrada, J.M., Arenas, R., Díez Fernández, R., González del Tánago, J., Martín-Parra, L.M., Matas, J., Rojo-Pérez, E., Sánchez Martínez, S., Andonaegui, P., Solis Alulima, B., 2021. Tectonic setting and isotopic sources (Sm–Nd) of the SW Iberian Autochthon (Variscan Orogen). J. Iber. Geol. 47, 121–150. https://doi.org/10.1007/s41513-020-00148-7.

Galadí-Enríquez, E., Galindo-Zaldívar, J., Simancas, F., Expósito, I., 2003. Diapiric emplacement in the upper crust of a granitic body: the La Bazana granite (SW Spain). Tectonophysics 361 (1–2), 83–96. https://doi.org/10.1016/S0040-1951(02)00562-0.

Gao, P., Zheng, Y.-F., Zhao, Z.-F., 2016. Distinction between S-type and peraluminous I-type granites: Zircon versus whole-rock geochemistry. Lithos 258–259, 77–91. https://doi.org/10.1016/j.lithos.2016.04.019.

García de Madinabeitia, S., Sánchez-Lorda, M.E., Gil Ibarguchi, J.I., 2008. Simultaneous determination of major to ultratrace elements in geological samples by fusion-dissolution and inductively coupled plasma mass spectrometry techniques. Anal. Chim. Acta 625 (2), 117–130. https://doi.org/10.1016/j.aca.2008.07.024.

Gerdes, A., Montero, P., Bea, F., Fershater, G., Borodina, N., Osipova, T., Shardakova, G., 2002. Peraluminous granites frequently with mantle-like isotope compositions: the continental-type Murzinka and Dzhabyk batholiths of the eastern Urals. Int. J. Earth Sci. 91 (1), 3–19. https://doi.org/10.1007/s005310100195.

Gómez-Frutos, D., Castro, A., Gutiérrez-Alonso, G., 2023. Post-collisional batholiths do contribute to continental growth. Earth Planet. Sci. Lett. 603, 117978 https://doi.org/10.1016/j.epsl.2022.117978.

Henriques, S.B.A., Neiva, A.M.R., Ribeiro, M.L., Dunning, G.R., Tajčmanová, L., 2015. Evolution of a Neoproterozoic suture in the Iberian Massif, Central Portugal: new U–Pb ages of igneous and metamorphic events at the contact between the Ossa Morena Zone and Central Iberian Zone. Lithos 220–223, 43–59. https://doi.org/10.1016/j.lithos.2015.02.001.

Jacob, J.-B., Moyen, J.-F., Fiannacca, P., Laurent, O., Bachmann, O., Janoušek, V., Farina, F., Villaros, A., 2021. Crustal melting vs. fractionation of basaltic magmas: part 2, Attempting to quantify mantle and crustal contributions in granitoids. Lithos 402-403, 106292. https://doi.org/10.1016/j.lithos.2021.106292.

Janoušek, V., Moyen, J.-F., 2020. Whole-rock geochemical modelling of granite genesis: the current state of play. Geol. Soc. Lond. Spec. Publ. 491, 267–291. https://doi.org/10.1144/SP491-2018-160.

Janoušek, V., Bonin, B., Collins, W.J., Farina, F., Bowden, P., 2020. Post-Archean granitic rocks: contrasting petrogenetic processes and tectonic environments. Geol. Soc. London Spec. Publ. 491, 1–8. https://doi.org/10.1144/SP491-2019-197.

López-Guijarro, R., Armendáriz, M., Quesada, C., Fernández-Suárez, J., Murphy, J.B., Pin, C., Bellido, F., 2008. Ediacaran–Palaeozoic tectonic evolution of the Ossa Morena and Central Iberian zones (SW Iberia) as revealed by Sm–Nd isotope

systematics. Tectonophysics 461 (1–4), 202–214. https://doi.org/10.1016/j.tecto.2008.06.006.
McDonough, W.F., Sun, S.-s., 1995. The composition of the Earth. Chem. Geol. 120 (3–4), 223–253. https://doi.org/10.1016/0009-2541(94)00140-4.
Miller, C.F., McDowell, S.M., Mapes, R.W., 2003. Hot and cold granites? Implications of zircon saturation temperatures and preservation of inheritance. Geology 31 (6), 529–532. https://doi.org/10.1130/0091-7613(2003)031<0529:HACGIO>2.0.CO;2.
Montel, J.-M., 1993. A model for monazite/melt equilibrium and application to the generation of granitic magmas. Chem. Geol. 110 (1–3), 127–146. https://doi.org/10.1016/0009-2541(93)90250-M.
Moyen, J.-F., Laurent, O., Chelle-Michou, C., Couzinié, S., Vanderhaeghe, O., Zeh, A., Villaros, A., Gardien, V., 2017. Collision vs. subduction-related magmatism: two contrasting ways of granite formation and implications for crustal growth. Lithos 277, 154–177. https://doi.org/10.1016/j.lithos.2016.09.018.
Moyen, J.-F., Janoušek, V., Laurent, O., Bachmann, O., Jacob, J.-B., Farina, F., Fiannacca, P., Villaros, A., 2021. Crustal melting vs. fractionation of basaltic magmas: part 1, granites and paradigms. Lithos 402–403, 106291. https://doi.org/10.1016/j.lithos.2021.106291.
Nabelek, P.I., 2020. Petrogenesis of leucogranites in collisional orogens. Geol. Soc. Lond. Spec. Publ. 491, 179–207. https://doi.org/10.1144/SP491-2018-181.
Ordoñez-Casado, B., 1998. Geochronological Studies of the Pre-Mesozoic Basement of the Iberian Massif: The Ossa Morena Zone and the Allochthonous Complexes within the Central Iberian Zone. PhD Thesis,. University of Zürich, Switzerland.
Ordoñez-Casado, B., Martin-Izard, A., García-Nieto, J., 2008. SHRIMP-zircon U–Pb dating of the Ni–Cu–PGE mineralized Aguablanca gabbro and Santa Olalla granodiorite: confirmation of an Early Carboniferous metallogenic epoch in the Variscan Massif of the Iberian Peninsula. Ore Geol. Rev. 34 (3), 343–353. https://doi.org/10.1016/j.oregeorev.2008.03.002.
Padilla, A.J., Gualda, G.A.R., 2016. Crystal-melt elemental partitioning in silicic magmatic systems: an example from the Peach Spring Tuff high-silica rhyolite, Southwest USA. Chem. Geol. 440, 326–344. https://doi.org/10.1016/j.chemgeo.2016.07.004.
Pereira, M.F., Chichorro, M., Solá, A.R., Silva, J.B., Sánchez-García, T., Bellido, F., 2011. Tracing the Cadomian magmatism with detrital/inherited zircon ages by in-situ U–Pb SHRIMP geochronology (Ossa-Morena Zone, SW Iberian Massif). Lithos 123 (1–4), 204–217. https://doi.org/10.1016/j.lithos.2010.11.008.
Pereira, M.F., Linnemann, U., Hofmann, M., Chichorro, M., Solá, A.R., Medina, J., Silva, J.B., 2012. The provenance of late Ediacaran and early Ordovician siliciclastic rocks in the Southwest Central Iberian Zone: constraints from detrital zircon data on northern Gondwana margin evolution during the late Neoproterozoic. Precambrian Res. 192–195, 166–189. https://doi.org/10.1016/j.precamres.2011.10.019.
Pereira, M.F., Chichorro, M., Moita, P., Santos, J.F., Solá, A.R., Williams, I.S., Silva, J.B., Armstrong, R.A., 2015. The multistage crystallization of zircon in calc-alkaline granitoids: U–Pb age constraints on the timing of Variscan tectonic activity in SW Iberia. Int. J. Earth Sci. 104, 1167–1183. https://doi.org/10.1007/s00531-015-1149-3.
Pichavant, M., Montel, J.-M., Richard, L.R., 1992. Apatite solubility in peraluminous liquids: experimental data and an extension of the Harrison–Watson model. Geochim. Cosmochim. Acta 56 (10), 3855–3861. https://doi.org/10.1016/0016-7037(92)90178-L.
Robb, L., 2020. Introduction to Ore-Forming Processes, 2nd ed. Wiley-Blackwell, Oxford.
Rodríguez, C., Pereira, M.F., Castro, A., Gutiérrez-Alonso, G., Fernández, C., 2022. Variscan intracrustal recycling by melting of Carboniferous arc-like igneous protoliths (Évora Massif, Iberian Variscan belt). Geol. Soc. Am. Bull. 134 (5–6), 1549–1570. https://doi.org/10.1130/B36111.1.
Rojo-Pérez, E., Fuenlabrada, J.M., Linnemann, U., Arenas, R., Sánchez Martínez, S., Díez Fernández, R., Martín Parra, L.M., Matas, J., Andonaegui, P., Fernández-Suárez, J., 2021. Geochemistry and Sm–Nd isotopic sources of Late Ediacaran siliciclastic series in the Ossa–Morena Complex: Iberian–Bohemian correlations. Int. J. Earth Sci. 110, 467–485. https://doi.org/10.1007/s00531-020-01963-0.
Romeo, I., Capote, R., Tejero, R., Lunar, R., Quesada, C., 2006. Magma emplacement in transpression: the Santa Olalla Igneous complex (Ossa-Morena Zone, SW Iberia). J. Struct. Geol. 28 (10), 1821–1834. https://doi.org/10.1016/j.jsg.2006.06.007.
Rudnick, R.L., Gao, S., 2014. Composition of the Continental Crust. In: Holland, H.D., Turekian, K.K. (Eds.), Treatise on Geochemistry, , 2nd edvol. 4. The Crust. Elsevier Science, Oxford. https://doi.org/10.1016/B978-0-08-095975-7.00301-6.
Sánchez-García, T., Quesada, C., Bellido, F., Dunning, G.R., González del Tánago, J., 2008. Two-step magma flooding of the upper crust during rifting: the early Paleozoic of the Ossa Morena Zone (SW Iberia). Tectonophysics 461 (1–4), 72–90. https://doi.org/10.1016/j.tecto.2008.03.006.
Sánchez-García, T., Bellido, F., Pereira, M.F., Chichorro, M., Quesada, C., Pin, C., Silva, J.B., 2010. Rift-related volcanism predating the birth of the Rheic Ocean (Ossa-Morena zone, SW Iberia). Gondwana Res. 17 (2–3), 392–407. https://doi.org/10.1016/j.gr.2009.10.005.
Sánchez-Lorda, M.E., Sarrionandia, F., Ábalos, B., Carracedo, M., Eguíluz, L., Gil Ibarguchi, J.I., 2014. Geochemistry and paleotectonic setting of Ediacaran metabasites from the Ossa-Morena Zone (SW Iberia). Int. J. Earth Sci. 103, 1263–1286. https://doi.org/10.1007/s00531-013-0937-x.
Sánchez-Lorda, M.E., Ábalos, B., García de Madinabeitia, S., Eguíluz, L., Gil Ibarguchi, J.I., Paquette, J.-L., 2016. Radiometric discrimination of pre-Variscan amphibolites in the Ediacaran Serie Negra (Ossa-Morena Zone, SW Iberia). Tectonophysics 681, 31–45. https://doi.org/10.1016/j.tecto.2015.09.020.
Sarrionandia, F., 2006. Estudio petrológico del complejo plutónico de Valencia del Ventoso (Badajoz). PhD Thesis,. University of the Basque Country, Spain.
Sarrionandia, F., Carracedo Sánchez, M., Eguíluz, L., Ábalos, B., Rodríguez, J., Pin, C., Gil Ibarguchi, J.I., 2012. Cambrian rift-related magmatism in the Ossa-Morena Zone (Iberian Massif): geochemical and geophysical evidence of Gondwana break-up. Tectonophysics 570–571, 135–150. https://doi.org/10.1016/j.tecto.2012.07.023.
Sarrionandia, F., Ábalos, B., Errandonea-Martin, J., Eguíluz, L., Santos-Zalduegui, J.F., García de Madinabeitia, S., Carracedo-Sánchez, M., Gil Ibarguchi, J.I., 2020. Ediacaran - Earliest Cambrian arc-tholeiite and adakite associations of the Malcocinado Formation (Ossa-Morena Zone, SW Spain): Juvenile continental crust and deep crustal reworking in northern Gondwana. Lithos 372–373, 105683. https://doi.org/10.1016/j.lithos.2020.105683.
Sarrionandia, F., Errandonea-Martin, J., Larrondo, E., Carracedo-Sánchez, M., Ábalos, B., Gil Ibarguchi, J.I., 2023. Low-Ti continental tholeiite origin of magmas with calc-alkaline signature in transcurrent settings: the Mississippian Matachel volcanic field (SW Iberian Massif). Geochem. Geophys. Geosyst. 24 (11), e2023GC011139 https://doi.org/10.1029/2023GC011139.
Schiller, D., Finger, F., 2019. Application of Ti-in-zircon thermometry to granite studies: problems and possible solutions. Contrib. Mineral. Petrol. 174, 51. https://doi.org/10.1007/s00410-019-1585-3.
Shand, S.J., 1943. Eruptive Rocks. Their Genesis, Composition, Classification, and their Relation to Ore-Deposits with a Chapter on Meteorite. John Wiley and Sons, New York.
Siégel, C., Bryan, S.E., Allen, C.M., Gust, D.A., 2018. Use and abuse of zircon-based thermometers: a critical review and a recommended approach to identify antecrystic zircons. Earth Sci. Rev. 176, 87–116. https://doi.org/10.1016/j.earscirev.2017.08.011.
Solá, A.R., 2007. Relaçoes petrogeoquímicas dos maciços graníticos do NE Alentejano. PhD Thesis,. University of Coimbra, Portugal.
Solá, A.R., Pereira, M.F., Williams, I.S., Ribeiro, L.M., Neiva, A.M.R., Montero, P., Bea, F., Zinger, T., 2008. New insights from U–Pb zircon dating of Early Ordovician magmatism on the northern Gondwana margin: the Urra Formation (SW Iberian Massif, Portugal). Tectonophysics 461 (1–4), 114–129. https://doi.org/10.1016/j.tecto.2008.01.011.
Sylvester, P.J., 1998. Post-collisional strongly peraluminous granites. Lithos 45 (1–4), 29–44. https://doi.org/10.1016/S0024-4937(98)00024-3.
Tornos, F., Galindo, C., Casquet, C., Rodríguez Pevida, L., Martínez, C., Martínez, E., Velasco, F., Iriondo, A., 2006. The Aguablanca Ni–(Cu) sulfide deposit, SW Spain: geologic and geochemical controls and the relationship with a midcrustal layered mafic complex. Mineral. Deposita 41, 737–769. https://doi.org/10.1007/s00126-006-0090-6.
Villaseca, C., Barbero, L., Herreros, V., 1998. A re-examination of the typology of peraluminous granite types in intracontinental orogenic belts. Trans. R. Soc. Edinb. Earth Sci. 89 (2), 113–119. https://doi.org/10.1017/S0263593300007045.
Watson, E.B., Harrison, T.M., 1983. Zircon saturation revisited: temperature and composition effects in a variety of crustal magma types. Earth Planet. Sci. Lett. 64 (2), 295–304. https://doi.org/10.1016/0012-821X(83)90211-X.
Zen, E., 1988. Phase relations of peraluminous granitic rocks and their petrogenetic implications. Annu. Rev. Earth Planet. Sci. 16, 21–51. https://doi.org/10.1146/annurev.ea.16.050188.000321.